

**Research Articles: Systems/Circuits****Wide-area all-optical neurophysiology in acute brain slices**

Samouil L. Farhi<sup>1</sup>, Vicente J. Parot<sup>2,3</sup>, Abhinav Grama<sup>4,5</sup>, Masahito Yamagata<sup>4,5</sup>, Ahmed S. Abdelfattah<sup>6</sup>, Yoav Adam<sup>8</sup>, Shan Lou<sup>8</sup>, Jeong Jun Kim<sup>8</sup>, Robert E. Campbell<sup>6</sup>, David D. Cox<sup>4,5,7</sup> and Adam E. Cohen<sup>8,9,10</sup>

<sup>1</sup>Chemical Biology Program, Harvard University, Cambridge, Massachusetts, USA

<sup>2</sup>Biophysics Program, Harvard University, Cambridge, Massachusetts, USA

<sup>3</sup>Division of Health Science and Technology, Massachusetts Institute of Technology, Cambridge, Massachusetts, USA

<sup>4</sup>Department of Molecular and Cellular Biology, Harvard University, Cambridge, Massachusetts, USA

<sup>5</sup>Center for Brain Science, Harvard University, Cambridge, Massachusetts, USA

<sup>6</sup>Department of Chemistry, University of Alberta, Edmonton, Alberta, Canada

<sup>7</sup>J.A. Paulson School of Engineering and Applied Sciences

<sup>8</sup>Department of Chemistry and Chemical Biology Harvard University, Cambridge, Massachusetts, USA

<sup>9</sup>Department of Physics, Harvard University, Cambridge, Massachusetts, USA

<sup>10</sup>Howard Hughes Medical Institute, Harvard University, Cambridge, Massachusetts, USA

<https://doi.org/10.1523/JNEUROSCI.0168-19.2019>

Received: 20 January 2019

Revised: 15 March 2019

Accepted: 1 April 2019

Published: 5 April 2019

---

**Author contributions:** S.F., V.P., J.J.K., R.E.C., D.C., and A.C. designed research; S.F., V.P., A.G., A.A., Y.A., S.L., and J.J.K. performed research; S.F., V.P., A.G., M.Y., A.A., Y.A., S.L., and J.J.K. contributed unpublished reagents/analytic tools; S.F., V.P., J.J.K., and A.C. analyzed data; S.F., V.P., and A.C. wrote the first draft of the paper; S.F., V.P., and A.C. edited the paper; S.F., V.P., and A.C. wrote the paper.

**Conflict of Interest:** The authors declare no competing financial interests.

We thank Vaibhav Joshi, Katherine Williams, and Melinda Lee for technical assistance. We thank Bernardo Sabatini for Rbp4-Cre mice, and Christopher Werley for assistance with the microscope design. We thank Daryl Lim for providing HiLo reconstruction code. Joshua Sanes provided support for the cloning of H2B-jRGECO1a. This work was supported by the Howard Hughes Medical Institute. SLF was supported by an NSF Graduate Research Fellowship. VJP was supported by a Becas Chile scholarship. Work in David Cox's lab was supported by IARPA (contract #D16PC00002) and the Mind Brain Behavior Faculty Award of Harvard.

**Correspondence should be addressed to** A.E.C. ([cohen@chemistry.harvard.edu](mailto:cohen@chemistry.harvard.edu))

**Cite as:** J. Neurosci 2019; 10.1523/JNEUROSCI.0168-19.2019

**Alerts:** Sign up at [www.jneurosci.org/alerts](http://www.jneurosci.org/alerts) to receive customized email alerts when the fully formatted version of this article is published.

Accepted manuscripts are peer-reviewed but have not been through the copyediting, formatting, or proofreading process.

1    **Wide-area all-optical neurophysiology in acute brain slices**

2    Samouil L. Farhi<sup>1,\*</sup>, Vicente J. Parot<sup>2,3\*</sup>, Abhinav Grama<sup>4,5</sup>, Masahito Yamagata<sup>4,5</sup>, Ahmed S. Abdelfattah<sup>6</sup>,  
3    <sup>11</sup>, Yoav Adam<sup>8</sup>, Shan Lou<sup>8</sup>, Jeong Jun Kim<sup>8</sup>, Robert E. Campbell<sup>6</sup>, David D. Cox<sup>4,5,7</sup>, & Adam E. Cohen<sup>8,9,10†</sup>

4  
5    <sup>1</sup>Chemical Biology Program, Harvard University, Cambridge, Massachusetts, USA; <sup>2</sup>Biophysics Program,  
6    Harvard University, Cambridge, Massachusetts, USA; <sup>3</sup>Division of Health Science and Technology,  
7    Massachusetts Institute of Technology, Cambridge, Massachusetts, USA; <sup>4</sup>Department of Molecular and  
8    Cellular Biology, Harvard University, Cambridge, Massachusetts, USA; <sup>5</sup>Center for Brain Science, Harvard  
9    University, Cambridge, Massachusetts, USA; <sup>6</sup>Department of Chemistry, University of Alberta,  
10   Edmonton, Alberta, Canada; <sup>7</sup>J.A. Paulson School of Engineering and Applied Sciences; <sup>8</sup>Department of  
11   Chemistry and Chemical Biology Harvard University, Cambridge, Massachusetts, USA; <sup>9</sup>Department of  
12   Physics, Harvard University, Cambridge, Massachusetts, USA; <sup>10</sup>Howard Hughes Medical Institute,  
13   Harvard University, Cambridge, Massachusetts, USA; <sup>11</sup>Present address: Janelia Farm Research Campus,  
14   Ashburn, Virginia, USA. \*These authors contributed equally to this work. †Correspondence should be  
15   addressed to A.E.C. ([cohen@chemistry.harvard.edu](mailto:cohen@chemistry.harvard.edu)).  
16  
17

18    **Abstract**

19    Optical tools for simultaneous perturbation and measurement of neural activity open the possibility of  
20   mapping neural function over wide areas of brain tissue. However, spectral overlap of actuators and  
21   reporters presents a challenge for their simultaneous use, and optical scattering and out-of-focus  
22   fluorescence in tissue degrade resolution. To minimize optical crosstalk, we combined an optimized  
23   variant (eTsChR) of the most blue-shifted channelrhodopsin reported to-date with a nuclear-localized  
24   red-shifted  $\text{Ca}^{2+}$  indicator, H2B-jRGECO1a. To perform wide-area optically sectioned imaging in tissue,  
25   we designed a structured illumination technique that uses Hadamard matrices to encode spatial  
26   information. By combining these molecular and optical approaches we made wide-area functional maps  
27   in acute brain slices from mice of both sexes. The maps spanned cortex and striatum and probed the  
28   effects of antiepileptic drugs on neural excitability and on the effects of AMPA and NMDA receptor  
29   blockers on functional connectivity. Together, these tools provide a powerful capability for wide-area  
30   mapping of neuronal excitability and functional connectivity in acute brain slices.

31    **Significance Statement**

32    A new technique for simultaneous optogenetic stimulation and calcium imaging across wide areas of  
33   brain slice enables high-throughput mapping of neuronal excitability and synaptic transmission.  
34

35    **Introduction**

36    All-optical neurophysiology (AON)—simultaneous optical stimulation and optical readout of neural  
37   activity—provides a promising approach to mapping neural excitability and functional connectivity  
38   across wide regions of brain tissue (Emiliani et al., 2015; Ronzitti et al., 2017). Recent advances in two-  
39   photon (2P) calcium imaging AON *in vivo* have enabled measurement of neuronal population activity  
40   while stimulating or inhibiting up to ~100 near-surface neurons in small cortical regions (Shemesh et al.,  
41   2017; Ronzitti et al., 2017; Mardinly et al., 2018). However, most of the intact rodent brain remains  
42   inaccessible to optical microscopy, and one would ideally like to perform AON simultaneously on many  
43   thousands of neurons across multiple brain regions to map spatial variations in function or to detect  
44   rare sub-populations.

45       Acute brain slices in principle enable wide-area optical mapping across any brain region. While  
46   slicing cuts many long-range connections, the procedure is commonly used to investigate the molecular

47 makeup, electrophysiological properties, and local microcircuitry of the component neurons (Ting et al.,  
48 2018). Wide-area AON in acute slices would enable several types of new applications. Pharmacological  
49 studies with tool compounds could probe the distribution and functional roles of receptors or channels  
50 in the tissue, e.g. to characterize the nature of synaptic connections between specific brain regions; or  
51 to discover cell populations that expresses a receptor for an orphan ligand (see, e.g. (Jiang et al., 2015;  
52 Harnett et al., 2013; Blot and Barbour, 2014)). Tests with candidate drugs could probe the distribution  
53 and functional consequences of drug action. Further potential applications include probing the  
54 response of brain tissue to physical or chemical perturbations, e.g. to map responses to changes in  
55 nutrients, hormones, oxygen, or temperature. In all these applications, a large field of view (FOV) for  
56 simultaneous large-area imaging is essential because the sample response might adapt or degrade, and  
57 physiology may vary as a function of time post perturbation.

58 Brain slices typically show little spontaneous activity and obviously lack sensory inputs, so  
59 optical mapping in brain slices requires a means to evoke activity. Optogenetic stimulation can directly  
60 evoke activity in the measured neurons, or can activate axon terminals—even when the axons have  
61 been severed from the cell bodies—and evoke postsynaptic responses (Petreanu et al., 2007). Optical  
62 readouts of evoked response could reveal the spatial structure of intrinsic neuronal excitability, of  
63 functional connectivity, or of local microcircuit dynamics, and molecular or physical influences thereon.

64 The optical requirements of wide-area AON in brain slice differ from *in vivo*, suggesting that a  
65 distinct approach could be warranted. In brain slice there is a benefit to having a very wide field of view  
66 to probe many neurons and brain regions simultaneously. Optical sectioning is important to distinguish  
67 in-focus cells from background, but imaging deep ( $> 100 \mu\text{m}$ ) into the preparation is less important than  
68 *in vivo* because the plane of the slice can expose any brain structure of interest. One may wish to  
69 stimulate many thousands of cells simultaneously, a task beyond the capabilities of current 2P  
70 stimulation techniques. If one treats cells as units, the spatial resolution must be sufficient to resolve  
71 single cells, but need not resolve fine sub-cellular structures. Time resolution must be sufficient to  
72 resolve dynamics slice wide, typically  $< 200 \text{ ms}$  for  $\text{Ca}^{2+}$  imaging. These factors, discussed in detail  
73 below, suggest that one-photon (1P) stimulation and imaging may be preferable over the 2P approaches  
74 which have been optimized for *in vivo* use. To achieve 1P AON in brain slice one must (a) identify an  
75 actuator/reporter pair with good photostability and minimal optical crosstalk under 1P illumination, and  
76 (b) implement a 1P optically sectioned wide-area imaging scheme. Here we combine molecular and  
77 optical engineering to address these challenges.

78 Red-shifted channelrhodopsins have been combined with a GCaMP  $\text{Ca}^{2+}$  indicator for 2P AON *in*  
79 *vivo* (Rickgauer et al., 2014; Packer et al., 2015; Carrillo-Reid et al., 2016), but 1P GCaMP excitation  
80 causes spurious channelrhodopsin excitation. Lower optical crosstalk is achieved by pairing a blue-  
81 shifted channelrhodopsin with a red-shifted reporter (Hochbaum et al., 2014). Red genetically encoded  
82  $\text{Ca}^{2+}$  indicators (RGEClIs) now offer good sensitivity, but their combination with optogenetic stimulation  
83 has been hampered by blue-light induced photoswitching of the mApple-based chromophores used in  
84 the most sensitive RGEClIs (Akerboom et al., 2013; Inoue et al., 2015; Dana et al., 2016). Furthermore,  
85 blue channelrhodopsins such as Chr2(H134R) retained some excitation at the yellow (561 nm)  
86 wavelengths used to excite RGEClIs, introducing crosstalk of the imaging light into the stimulation  
87 channel. A truly orthogonal 1P actuator/RGECl reporter pair has not previously been reported.

88 TsChR, derived from *Tetraselmis striata* (Klapoetke et al., 2014), is the most blue-shifted  
89 channelrhodopsin reported to-date, but its initial characterization yielded a poor photocurrent. To our  
90 knowledge, TsChR has not previously been used in any optogenetic experiments. Here we show that a  
91 version with improved trafficking, eTsChR, drives robust spiking in cultured neurons and in tissue.  
92 Combination of eTsChR with a nuclear-localized red-shifted  $\text{Ca}^{2+}$  reporter, H2B-jRGECO1a, achieved 1-  
93 photon AON in cultured neurons and in slice. The blue light used to activate the eTsChR was dim

94 enough to avoid jRGECO1a photoswitching, and the yellow light used to excite jRGECO1a did not  
95 spuriously activate the eTsChR.

96 On the imaging front, 1P structured illumination microscopy (SIM) techniques can achieve  
97 optical sectioning in tissue (Mertz, 2011). We developed a generalized SIM technique based on  
98 Hadamard-Walsh encoding and implemented it in a mesoscope imaging system. Hadamard microscopy  
99 provides better rejection of out-of-plane fluorescence than do other SIM techniques and offers the  
100 ability to make systematic tradeoffs between background rejection and time resolution.

101 By applying 1P optogenetic stimulation and Hadamard microscopy to acute slices expressing  
102 eTsChR and H2B-jRGECO1a, we obtained simultaneous functional characterization of > 6,000 neurons,  
103 spread over a region 2.3 x 2.3 mm with 5.6 Hz time resolution. Maps of optically induced activity  
104 highlighted distinct cortical layers, which otherwise appeared homogeneous in their fluorescence. We  
105 used the AON system to map with cellular resolution the effects of anti-epileptic drugs on neural  
106 excitability, and to study cortico-cortico and cortico-striatal functional connectivity. Finally, we show  
107 that with an improvement to the algorithm based on compressed sensing, the imaging speed can be  
108 increased to 33 Hz (Parot et al., 2019). The combined molecular and optical tools provide a powerful  
109 system for wide-area investigations of neural function in brain tissue.

110  
111 **Materials and methods**  
112

113 **DNA constructs.** R-CaMP2 was a gift from Haruhiko Bito. TsChR was a gift from Ed Boyden. jRGECO1a  
114 and jRCAMP1a were obtained from Addgene (Plasmids #61563 and #61562). All RGECLs were cloned  
115 between the BamHI and EcoRI sites of the backbone from FCK-Arch-GFP (Addgene Plasmid #22217) for  
116 expression in cultured neurons and for lentiviral production. For photophysical characterization, RGECLs  
117 were also cloned into an analog of the FCK vector replacing the CaMKII $\alpha$  promoter with a CAG promoter,  
118 a configuration we refer to as FCAG. The jRCAMP1a and jRGECO1a constructs included the nuclear  
119 export sequences found in the original publication(Dana et al., 2016). For nuclear localization, the  
120 nuclear export sequence of jRGECO1a was replaced with an H2B tag, and cloned into an AAV-hSyn-DO  
121 Cre-off vector. TsChR, including an N-terminal Kir2.1 trafficking sequence followed by a GFP fluorescent  
122 tag, was cloned into FCK and into an AAV expression vector under control of the human synapsin  
123 promoter (AAV-hSyn). CheRiff-TS-GFP (Addgene Plasmid # 51693) was cloned into an AAV-CAG-DIO  
124 expression vector. FCK-ChR2(H134R)-GFP was used as a reference for eTsChR characterization. FCK-VSV-  
125 G (Addgene Plasmid #8454) and psPAX2 (Addgene Plasmid #12260) were used in lentiviral production.  
126 pUC19 (NEB #N3041) was used as a diluent in calcium phosphate transfections.

127  
128 **Cell culture and gene expression.**

129 *HEK cell culture and gene expression.* Photophysical measurements of RGECLs were performed in  
130 HEK293T cells (ATCC CRL-11268) cultured as previously described (Hochbaum et al., 2014). Cells were  
131 grown at 37 °C, 5% CO<sub>2</sub> in DMEM containing 10% FBS (Life Technologies 10082-147) and 50 U/mL  
132 penicillin-streptomycin (Life Technologies 15060-063). Cells were split with trypsin-EDTA (Life  
133 Technologies 25300054) every 2-3 days and used before passage 25. For gene delivery, cells were grown  
134 to 70% confluence in 24 well plates or 35 mm plastic dishes. 200 ng (for 24 well plates) or 400 ng (for 35  
135 mm plastic dishes) of FCAG-RGECL DNA was transfected using TransIT-293 (Mirus 2705) following  
136 manufacturer instructions. After 24 hours, cells were split onto Matrigel (Fisher Scientific 356234)  
137 coated glass bottom plates (In Vitro Scientific D35-14-1.5-N) and imaged 24 hours later.

138  
139 *Low titer lentivirus production.* HEK293T cells were cultured as in the previous section, except that cells  
140 were split daily and the cell density was always maintained between 30 and 70%. Prior to P11, cells were  
141 split onto gelatin coated plates, prepared by incubating 15 cm plastic dishes (Nunc) for 20 minutes at

142 room temperature with 10 mL EmbryoMax 0.1% Gelatin solution (Millipore FS-006-B) and aspirating to  
143 dryness. 10 cm dishes were also used, and all amounts were scaled to the smaller surface area. After  
144 cells reached 80% confluence, cells were switched to 16 mL pre-warmed DMEM without FBS for 1-2  
145 hours. For each dish, the following were added, in order, to 1.2 mL DMEM: 14 µg of FCK-RGECI plasmid,  
146 9 µg psPAX2, and 4 µg VsVg were combined with 36 µL of 1 mg/mL PEI in water (Aldrich #408727). The  
147 tube was vortexed and incubated at room temperature for 10 minutes. The mixture was then pipetted  
148 dropwise over the surface area of the dish and the cells were returned to the incubator for 4 hours.  
149 After the incubation, the medium was replaced with 16 mL DMEM + 10% FBS without antibiotics. 36-48  
150 hours later, the medium was collected and centrifuged for 5 min at 500 × g. The supernatant was  
151 filtered through a 0.45 µm filter blocked with DMEM + 10% FBS and aliquoted in 1-5 mL fractions.  
152 Aliquots were kept at -80°C until use.

153  
154 *Primary neuron culture and gene expression.* Cultured rat hippocampal neurons on astrocyte  
155 monolayers were prepared as previously described (Hochbaum et al., 2014), with two modifications: (1)  
156 In Vitro Scientific dishes model D35-14-1.5-N were used instead of D35-20-1.5-N, while keeping the cell  
157 densities the same, and (2) neurons were cultured in Neurobasal-A (Life Technologies 10888-022)  
158 supplemented with B27 (Life Technologies 17504044) instead of Brainbits' NbActiv4. For  
159 electrophysiological and AON measurements, neurons were transfected via calcium phosphate, as  
160 previously described (Hochbaum et al., 2014) on DIV7 and used on DIV14-16. For comparison of RGECI  
161 performance by field stimulation (Fig. 1b,c), cultured neurons were lentivirally transduced. On DIV 7,  
162 half of the media from each dish (1 mL) was reserved and replaced with 250 µL of low titer FCK-RGECI  
163 lentivirus. After two days, all of the media was removed and replaced with the reserved media  
164 supplemented with an additional 1 mL of Neurobasal-A + B27 supplement.

165  
166 **Imaging and electrophysiology in culture**

167 *Microscope.* A custom-built epifluorescence microscope was used for measurements in HEK293T cells  
168 and in cultured neurons. Illumination was provided by a 561 nm 100 mW laser (Cobolt Jive 0561-04-01-  
169 0100-500) or a 488 nm 100 mW laser (Coherent Obis 1226419). The laser lines were combined and  
170 focused in the back focal plane of the objective (Olympus Fluor 4x 0.24 NA for single action potential  
171 measurements of RGECIs; Olympus LCPlanFL 20x 0.40 NA for RGECI photobleaching measurements;  
172 Olympus UPlanSApo 10x 0.40 NA for RGECI photoswitching characterization; Olympus ApoN 60x 1.49 NA  
173 Oil for eTsChR characterization). Fast modulation of the 488 nm laser was achieved with an acousto-  
174 optic tunable filter (Gooch&Housego TF525-250-6-4-GH18A). Both laser lines were additionally  
175 modulated by neutral density filters as necessary. Fluorescence light was separated from illumination  
176 light using a quadband dichroic (Semrock Di01-R405/488/561/635). HQ550/50m or ET595/50 bandpass  
177 emission filters (Chroma) were used to isolate GFP or RGECI fluorescence, respectively, before capturing  
178 on a scientific CMOS camera (Hamamatsu Orca Flash 4.0). For photobleaching measurements, an  
179 additional 1 OD filter was inserted in the imaging path to avoid saturating the camera. Illumination  
180 profiles were acquired on bead samples before experiments each day and spot size was determined  
181 using a  $1/e^2$  cutoff. Laser powers were measured at the sample plane. A digital acquisition (DAQ) card  
182 (National Instruments PCIe 6259) was used to synchronize command and recording waveforms. Imaging  
183 frame rates and illumination powers are indicated in figure captions for each experiment.

184  
185 *Imaging and electrical recordings.* In all imaging measurements, culture medium was replaced with  
186 imaging buffer containing, in mM, 125 NaCl, 2.5 KCl, 2.5 HEPES, 30 glucose, 1 MgCl<sub>2</sub>, 3 CaCl<sub>2</sub>. The buffer  
187 pH was adjusted to 7.3 and osmolarity was 310 mOsm. Measurements were carried out at room  
188 temperature. 10 µM CNQX, 20 µM gabazine, and 25 µM APV (all Tocris) were included in cultured  
189 neuron experiments to block synaptic transmission. Channelrhodopsin characterization measurements

190 were performed in synaptic blockers with the addition of 1  $\mu$ M tetrodotoxin (Tocris). No additional all-  
191 trans retinal was added.

192 Field stimulation (**Fig. 1b,c**) was performed by inserting two chlorided silver wire loops 2 cm  
193 apart into the glass-bottomed imaging dish, touching the plastic on either side of the coverslip. A high  
194 voltage amplifier (Krohn-hite 7600M) was used to amplify 1 ms pulses generated by the DAQ card to 60-  
195 120 V. 3-4 FOVs were acquired for each construct, using a fresh dish each time.

196 For patch clamp electrophysiology measurements (**Fig. 1e-g, Fig. 9d**), 3-5 M $\Omega$  borosilicate glass  
197 pipettes (WPI) were filled with internal solution containing, in mM, 125 potassium gluconate, 8 NaCl, 0.6  
198 MgCl<sub>2</sub>, 0.1 CaCl<sub>2</sub>, 1 EGTA, 10 HEPES, 4 Mg-ATP, 0.4 Na-GTP, adjusted to pH 7.5 and 295 mOsm with  
199 sucrose. Voltage- and current-clamp recordings were obtained with a Multiclamp 700B amplifier  
200 (Molecular Devices) while illuminating with 1 s 488 nm pulses or 2s 561 nm pulses of intensities  
201 indicated in figure captions. In voltage clamp measurements, cells were held at -65 mV. In current-clamp  
202 measurements, an offset current was injected to maintain the resting membrane potential at -65 mV.  
203 Signals were filtered at 5 kHz with the amplifier's internal Bessel filter and digitized at 10 kHz.

204

205 *Data analysis.* All values are expressed as mean  $\pm$  standard error of the mean (s.e.m.). *P* values were  
206 obtained from Student's *t*-tests unless otherwise indicated.

207 Whole FOV RGECl single action potential responses (**Fig. 1b,c, Table 1**) were extracted as  
208 previously described (Chen et al., 2013). Activation time constants were extracted from  
209 monoexponential fits between stimulation onset and maximum  $\Delta F/F$ . For inactivation time constants,  
210 the fluorescence trace after the maximum  $\Delta F/F$  was fit to a sum of two exponential decays, and the  $\tau_{off}$   
211 was taken as the time for the fit to decay to half its maximum value. Photobleaching traces (**Table 1**)  
212 were extracted from separate cells and fit to a monoexponential to obtain time constant  $\tau_{bleach}$ .

213 Movies of blue light photoswitching (**Fig. 2d,e**) were preprocessed to reject saturated pixels and  
214 a threshold equal to half the average of movie was used to separate foreground from background.  
215 Background intensity was subtracted from the original movies and the averages of the resulting  
216 foreground traces (combining 10-20 cells each) were used in downstream analysis. Traces were  
217 converted to  $\Delta F/F$  using the fluorescence value before blue light stimulation as  $F_0$ . "Photoswitching  
218  $\Delta F/F$ " was defined as the  $\Delta F/F$  immediately after blue light illumination ends (**Fig. 2d**, inset).

219 For comparison of channelrhodopsins (**Fig. 1e-g, Fig. 9d**), cells were rejected if they required  
220 >100 pA holding current to maintain -65 mV in current clamp or if their baselines drifted by more than  
221 the smallest steady state photocurrent amplitude in voltage clamp mode. Steady-state 488 nm  
222 photocurrents were extracted as the average photocurrent over the last 100 ms of blue light  
223 illumination. Steady state 561 nm photocurrents and depolarizations were extracted from 1 s of data.  
224 On time constants were obtained from single exponential fits to the first 1.5 ms of 488 nm illumination.  
225 Off time constants were obtained from single exponential fits to the 99.5 ms following blue light 488  
226 illumination.

227 Recordings of jRGECO1a fluorescence in **Fig. 1h** were corrected for photobleaching with a bi-  
228 exponential fit to the initial period in each movie, before stimulation, while recordings of BeRST1  
229 fluorescence were corrected for photobleaching by a sliding, 1000 point, median filter. Both traces were  
230 converted to  $\Delta F/F$  based on the fluorescence before blue light stimulation. Frames acquired during blue  
231 light stimulation were dropped to avoid optical crosstalk.

232

### 233 **Hadamard imaging**

234 *Microscope.* In the ultra-widefield microscope (**Fig. 3a**), a 561 nm laser beam (MPB Communications F-  
235 04306-02) was transmitted through a rotating diffuser, and merged with a 470 nm LED beam (Thorlabs  
236 M470L3). Both were expanded, focused, and coupled through free space to fill with high NA illumination

237 a digital micromirror device (DMD) module (Vialux V-7001; 1024x768 pixels, 13.7  $\mu\text{m}$  pitch). Multiple  
238 diffraction orders emitted from the DMD pattern were transmitted by a 100 mm projection tube lens  
239 (Zeiss Makro-Planar 100 mm, L1 in **Fig. 3a**), reflected off a custom dichroic mirror (Semrock Di01-  
240 R405/488/561/635-t3-60x85), and imaged onto the sample by a 50 mm objective lens (Olympus  
241 MVPLAPO 2XC, NA 0.5, L2 in **Fig. 3a**). The 3 mm substrate thickness of the dichroic mirror minimized  
242 warping-induced projection aberrations. Fluorescence emission was collected through the same  
243 objective and dichroic, a large diameter (60mm) emission filter (Semrock FF01-520/35-60-D or Chroma  
244 ET600/50m, F in **Fig. 3a**), and a 135 mm imaging tube lens (Zeiss Apo-Sonnar 135 mm, L3 in **Fig. 3a**) onto  
245 a scientific CMOS camera (Hamamatsu Orca Flash 4.0, 2048x2048 pixels). The FOV was 4.6x4.6  $\text{mm}^2$  in  
246 the sample plane, corresponding to a magnification of 2.89x onto the camera, and 2.17x onto the DMD.  
247 Camera and DMD pixels were 2.25  $\mu\text{m}$  and 6.3  $\mu\text{m}$  wide in the sample, respectively. Hardware and  
248 triggers were programmed in LabView, with pattern generation and data analysis performed in MATLAB.  
249

250 *Illumination patterns.* To reject light scattered within the sample, pattern sequences were designed such  
251 that in the projected series of 2D images, neighboring locations of the sample were illuminated with  
252 orthogonal functions of intensity vs. time. A Hadamard matrix,  $H$ , of size  $m$  is a binary square matrix  
253 with elements  $\{-1,1\}$  that fulfills  $H^T H = mI_m$ , where  $I_m$  is the identity matrix of size  $m$ ; its normalized  
254 form has value 1 in the first column and first row. Illumination intensities could not be negative, so the  
255 projected intensity patterns were defined as  $P = (H' + 1)/2$  where  $H' = H[1, \dots, m; m - n + 1, \dots, m]$   
256 was an incomplete orthogonal basis given by the last  $n$  columns of a normalized Hadamard matrix, with  
257  $n < m$ .

258 The illumination patterns  $P$  thus had binary values  $\{0,1\}$  corresponding to DMD mirror positions  
259 OFF and ON respectively. Each location was illuminated with a positive temporal function orthogonal to  
260 all other designed Hadamard codes, as verified by  $P^T H' = I_n * m/2$ . For a given number of locations, a  
261 Hadamard matrix provided a set of shortest possible binary orthogonal functions. To arrange the  $n$   
262 codes in  $P$  into illumination patterns,  $m = n + 1$  images were defined assigning code  $k_{i,j} \in \{1..n\}$  to  
263 DMD pixel  $(i,j)$ , as  $k_{i,j} = \text{mod}(i * q + j, n) + 1$ , where  $q$  was an offset parameter that maximized  
264 spatial separation of repeated codes.  $(n, q)$  was set to (11,3) for functional imaging, and to (63,14) or  
265 (59,8) for structural imaging. To further reduce spurious scattering cross-talk, a random binary mask  $R$   
266 was generated to flip the sign of 50% of DMD pixels, applied as an exclusive OR operation on all DMD  
267 patterns against the same mask  $R$ . In the compressed sensing experiment (**Fig. 10**) the sequence of  
268 Hadamard patterns was interleaved with its complement (interchanging bright and dark pixels).  
269

270 *Calibration.* To prepare the system for each imaging session, a calibration data-set  $C$  was obtained by  
271 placing a thin fluorescent sample at the focal plane, and acquiring an image with each illumination  
272 pattern. The sample consisted of green or orange neon Sharpie (Newell Brands, NJ) ink painted on (or  
273 sandwiched between) glass coverslips, to match imaging conditions of subsequent acute (fixed) tissue  
274 experiments. For each camera pixel, the time series of its photon counts was cross-correlated against  
275 each Hadamard sequence as  $C^T H'$ . The resulting cross-correlation images displayed sharp peaks  
276 indicating the projected DMD locations for each code, with positive or negative correlation given by  $R$ . A  
277 synthetic approximation to the cross-correlation maps was calculated by finding the code with  
278 maximum absolute correlation for each pixel, yielding homogeneous, noise-free cross-correlation maps.  
279

280 *Reconstruction.* A Hadamard sequence data-set  $D$  was acquired after replacing the calibration sample  
281 with a tissue sample. Photon counts at each camera pixel were cross-correlated against each Hadamard  
282 sequence as  $D^T H'$ . Cross-correlation images displayed a set of peaks modulated by the local  
283 fluorophore density, and broadened by off-focus fluorescence and light scattering in the sample. Each  
284 peak characterized the scattering function of the corresponding tissue location, i.e. its absolute value

285 represents the image one would record with an illumination spot focused solely at that location in the  
 286 tissue. The next step was to apply a set of computational ‘pinholes’ to select the unscattered in-focus  
 287 photons, and to reject all others. The spatial filter was implemented through the element-wise product  
 288 of calibration correlation maps and tissue correlation maps, resulting in the positive filtered maps  
 289  $F = C^T H' \circ D^T H'$ . This computational process was akin to sifting emitted light through an array of  
 290 pinholes as happens physically in spinning disk confocal microscopy. The final computation step was to  
 291 aggregate the unscattered light by direct sum of the filtered images over all code maps, defining an  
 292 optical section image  $\phi_i = \sum_{k=1}^n F_{i,k}$ .

293 *Compressed Hadamard Imaging:* While this manuscript was in review, we developed a compressed  
 294 sensing measurement method to increase the time resolution from  $m$  camera frames (where  $m$  is the  
 295 length of the Hadamard sequence) to 2 camera frames per optical section. This approach and its trade-  
 296 offs are characterized elsewhere (Parot et al., 2019). For application of compressed Hadamard imaging  
 297 to AON (**Fig. 10**), procedures, optogenetic methods, and imaging protocol were as in other experiments,  
 298 except an Olympus XLPLN10XSVMP (NA= 0.6) objective was used to map DMD and camera pixel size to  
 299 2.52 and 0.9  $\mu\text{m}$  at the sample respectively. Illumination comprised 24 patterns, interleaved with their  
 300 complements, repeated in 36 cycles. Camera and DMD frames were updated at 66 Hz. Reconstruction  
 301 was performed in 64x64 pixel blocks with 40 principal components per block.

302  
 303 All static Hadamard image computations in this work were accelerated by computing  $\phi_i = \sum_{k=1}^m G_{i,k}$ ,  
 304 with  $G = C^T \circ D^T$ . This approach is numerically equivalent to the more involved process described  
 305 above, as proved by:

$$\begin{aligned} 306 \quad \phi_i &= \sum_{k=1}^n F_{i,k}, \\ 307 &= \sum_{k=1}^n \sum_{p=1}^m C_{i,p} H_{k,p} \sum_{q=1}^m D_{i,q} H_{k,q}, \\ 308 &= \sum_{p=1}^m \sum_{q=1}^n C_{i,p} D_{i,q} \sum_{k=1}^n H_{k,p} H_{k,q}, \\ 309 &= \sum_{p=1}^m \sum_{q=1}^n C_{i,p} D_{i,q} \delta_{p,q}, \\ 310 &= \sum_{q=1}^m C_{i,q} D_{i,q}, \\ 311 &= \sum_{k=1}^m G_{i,k}, \end{aligned}$$

312 where  $\delta_{p,q}$  is a Kronecker delta. The resulting optical section preserved unscattered light emitted from  
 313 the focal plane, while rejecting scattered light and background emissions. Standard wide-field  
 314 epifluorescence images were also computed from each Hadamard dataset by computing a direct sum of  
 315 all frames in the raw images,  $W_i = \sum_{k=1}^m D_{i,k}$ .

316 To correct for slight motion artifacts due to sample drift, all datasets from one brain slice were  
 317 registered to a reference image using a b-splines transform maximizing mutual information (Klein et al.,  
 318 2010).

319  
 320 *Hadamard image formation.* To understand the optical sectioning process, Hadamard microscopy was  
 321 modeled as an incoherent illumination, intensity-linear space-invariant optical system, in which the  
 322 intensity after propagation is given by a convolution between intensity before propagation and an  
 323 intensity impulse response function. In a discrete representation, the circulant convolution matrix  $S_1^T$   
 324 represented three-dimensional excitation intensity at the object, in response to an impulse function  
 325 reflectance at the DMD plane (turning on one DMD pixel). Similarly,  $S_2$  was defined as the intensity  
 326 collected by an impulse detector at the camera plane from emitted fluorescence in a three-dimensional  
 327 object (analogous to detection from one camera pixel). The data collected from tissue with fluorophore  
 328 distribution  $G$  upon illumination with a structured illumination pattern  $P$  was represented as  $D =$   
 329  $S_2 \text{ diag } G S_1^T P$ , where diag denoted rearrangement between vector and diagonal matrix. Calibration  
 330 with a thin uniform fluorescent object and no scattering was represented as  $C = P$ . After assuming that

332  $P$  contains an orthonormal Hadamard code with no spatial repetition, it followed that  $C^T H' = I_n$ , and  
 333  $D^T H' = S_2 \text{diag } G S_1^T I_n$ . Then  $\phi = \sum_k C^T H' \circ D^T H' = \text{diag}(S_2 \text{diag } G S_1^T)$ , or  $\phi = (S_1 \circ S_2)G$ . The  
 334 reconstructed optical section  $\phi$  was proportional to the object  $G$  convolved with the confocal scattering  
 335 function  $S = S_1 \circ S_2$  that resulted from the element-wise product of the projection and collection  
 336 scattering functions. To simulate the effects of lateral sub-pixel offset between the DMD pixels and the  
 337 smaller camera pixels, we used a continuous space version of the model described above, defining the  
 338 diffraction-limited excitation and emission PSFs as Gaussian functions and convolving these PSFs by  
 339 square apertures representing the DMD and camera pixels, respectively. The system PSF was calculated  
 340 from the product of the excitation and emission PSFs.

341  
 342 *Image processing and filtering.* The lines between DMD pixels led to a periodic grid artifact in Hadamard  
 343 optical sections. A Gaussian stopband filter was used to attenuate these artifacts. The filter parameters  
 344 were not changed after initial set-up.

345 The size of the computational pinholes could be adjusted in software to trade optical signal level  
 346 for z-resolution. Tuning of pinhole sizes was achieved by applying a spatial Gaussian filter to the  
 347 calibration patterns, with  $\sigma = 5.6 \mu\text{m}$  for functional images, and  $\sigma = 3.4 \mu\text{m}$  for structural images. Further  
 348 increases in  $\sigma$  to sizes larger than the spacing of pinholes resulted in a continuous transition to wide-  
 349 field epifluorescence imaging.

350 An additional source of systematic error came from local inhomogeneity of illumination  
 351 patterns. While the projected patterns have 50% duty cycle on average, variations in local illumination  
 352 can change the relative contributions of in-plane signal and background, resulting in imperfect  
 353 background cancellation manifested as regions with periodic background artifacts. This effect was  
 354 minimized for Hadamard images in Fig. 5b,c by dividing raw tissue data by its low spatial frequency  
 355 component, calculated with a Gaussian filter with  $\sigma=22.5 \mu\text{m}$ . Images in all figures were linearly mapped  
 356 to grayscale setting 0 to black and saturating to white the 0.01 percentile of highest intensity values  
 357 unless otherwise indicated.

358  
 359 *Characterization.* We quantified the performance of Hadamard, stripe SIM, and HiLo optical sectioning  
 360 methods by three measurements. First, we measured the point spread functions by imaging 200 nm  
 361 fluorescent beads (Invitrogen F8763) embedded in 1.5% agarose gel. Second, we tested the in-plane  
 362 uniformity of optical sections by measuring a thin fluorescent plane of orange neon Sharpie (Newell  
 363 Brands, NJ) ink painted on a glass coverslip. Third, we acquired multi-plane images of an acute brain slice  
 364 expressing H2B-jRGECO1a to evaluate the imaging quality of each method in turbid tissue.

365 For the beads and plane experiments, illumination patterns for Hadamard codes of length 12,  
 366 together with striped illumination with period 4 pixels and 4 phases, were interleaved and repeat-  
 367 averaged to match total photons and photobleaching conditions across datasets. HiLo optical sections  
 368 were computed from the same patterns used for Hadamard imaging, using a photon-matched uniform  
 369 illumination image and a repeat-averaged structured image corresponding to one Hadamard pattern.  
 370 HiLo uses only a single random illumination pattern, and thus necessarily uses a non-uniform total  
 371 photon count across the sample. We used more total photons in HiLo optical sections to avoid  
 372 penalizing this method in the comparison. A series of images taken at  $\Delta z = 2.24 \mu\text{m}$  were acquired to  
 373 map the three dimensional PSF.

374 Hadamard images were calculated as  $\phi_i = \sum_{k=1}^m G_{i,k}$ , with  $G = C^T \circ D^T$ . Stripe SIM optical  
 375 sections were calculated as  $\phi = |\sum_{k=0}^{m-1} I_k e^{-i2\pi k/m}|$ , with  $m=4$ . HiLo optical sections were calculated  
 376 setting the wavelet filter  $\sigma = 0.75$ . DMD modulation grid artifacts were present in all datasets and were  
 377 not corrected. Widefield reference images were obtained by summing all patterns in the Hadamard  
 378 sequence.

379 Images of the homogeneous fluorescent plane were acquired following the same protocol as for  
380 the beads. The same flat field correction was applied to all datasets by subtracting the offset and  
381 dividing by the blurred intensity distribution of a focused widefield image. All datasets were filtered  
382 equally to reduce DMD grid artifacts. Within a region of interest, the standard deviation of values was  
383 normalized by their mean to obtain coefficients of variation.

384 To estimate the degree of cell-to-cell fluorescence crosstalk in nuclear-labeled acute brain slices,  
385 we first computed a mean Hadamard ‘nucleus spread function’, i.e. the mean fluorescence distribution  
386 measured from multi-plane structural Hadamard images of fluorescent nuclei in acute brain slices. We  
387 then used high-resolution confocal microscopy to estimate the center locations of all neuronal nuclei in  
388 a fixed brain slice up to a depth of 100  $\mu\text{m}$ . We computationally positioned the nucleus spread  
389 functions at the nuclear locations, adjusted signal levels to account for the measured attenuation with  
390 depth, and estimated the crosstalk, i.e. the amount of signal ascribed to each nucleus that originated  
391 from other nuclei.

392

### 393 Software accessibility

394 The Hadamard control and analysis software and an example data-set are available at:

395 <https://github.com/adamcohenlab/Hadamard-Code>

396 The compressed Hadamard analysis software is available at:

397 <https://github.com/adamcohenlab/Compressed-Hadamard-Code>

398

### 399 Animals and acute slice measurements

400 *Animals.* All procedures involving animals were in accordance with the National Institutes of Health  
401 Guide for the care and use of laboratory animals and were approved by the Institutional Animal Care  
402 and Use Committee (IACUC) at Harvard University. Excitability measurements and characterization of  
403 functional Hadamard imaging were performed in wild type C57Bl6 (Charles River Labs #027) mice.  
404 Functional connectivity assays were performed in Rbp4-Cre<sup>+/−</sup> mice donated by Bernardo Sabatini’s lab  
405 and originally generated in the GenSat project (#KL100). For structural imaging of membrane bound  
406 mCitrine, FLOXed Optopatch-3 mice (Jackson Labs #029679) were crossed with Rbp4-Cre<sup>+/−</sup> mice or with  
407 CaMK2a-Cre<sup>+/−</sup> mice (Jackson Labs, #005359).

408

409 *AAV injection.* AAV2/9-hSyn-DO-H2B-jRGECO1a ( $1.60 \times 10^{13}$  GC/mL) and AAV2/9-hSyn-eTsChR ( $2.22 \times 10^{13}$   
410 GC/mL) were produced at Massachusetts Eye and Ear Infirmary Vector Core. AAV2/9-CAG-DIO-CheRiff-  
411 TS-GFP ( $5.80 \times 10^{13}$  GC/mL) was produced by the Stanford Vector Core. AAV1-hSyn-NES-jRGECO1a  
412 ( $2.44 \times 10^{13}$  GC/mL) was purchased from the University of Pennsylvania Vector Core. When two viruses  
413 were coinjected, they were mixed in a one-to-one volume ratio. The final mixture was mixed in a 7:1  
414 ratio with 0.4% Trypan Blue to aid in visualization during injection. For viral injections, neonatal (P0-2)  
415 animals were cold-anesthetized and taped to an aluminum heatsink submerged in an ice bath, with their  
416 heads resting on a modeling clay support. A stereotaxic injector (WPI #UMC4) mounted on a stereotaxic  
417 frame (Stoelting) was used to inject virus 1.6 mm anterior and 1.6 mm lateral to lambda every 0.4 mm  
418 starting from 3 mm beneath the surface of the skull. 40 nL of virus was delivered at each depth at a rate  
419 of 5 nL/s. If only one virus was used, only 20 nL were injected per depth. Expression levels were  
420 sufficiently high for Hadamard imaging from 12 days until at least 9 weeks after injection.

421

422 *Preparation of fixed slices.* Fresh 300 $\mu\text{m}$  brain sections were incubated in 4% paraformaldehyde  
423 overnight at 4 °C, then mounted on a glass slide in Fluoromount and stored at 4 °C.

424

425 *Acute slice preparation and imaging.* Acute slices were prepared from P21-28 animals. Animals were  
426 deeply anesthetized via isoflurane inhalation and transcardially perfused with ice-cold choline cutting

427 solution, containing, in mM 110 choline chloride, 25 sodium bicarbonate, 2.5 potassium chloride, 7  
428 magnesium chloride, 0.5 calcium chloride, 1.25 monobasic sodium phosphate, 25 glucose, 11.6 ascorbic  
429 acid, and 3.1 pyruvic acid (310 mOsm/kg). The brain was blocked with one coronal cut just anterior to  
430 the tectum and mounted with Krazy glue on the specimen disk of a Leica VT1200s vibratome. After  
431 mounting, hemispheres were separated with a sagittal cut down the midline of the brain. The brain was  
432 covered with more ice-cold choline solution and then sliced in 300  $\mu$ m steps. Slices containing the  
433 striatum were recovered for 45 minutes in a 34 °C artificial-cerebrospinal fluid (ACSF) bath containing, in  
434 mM, 125 NaCl, 2.5 KCl, 25 NaHCO<sub>3</sub>, 2 CaCl<sub>2</sub>, 1 MgCl<sub>2</sub>, 1.25 NaH<sub>2</sub>PO<sub>4</sub>, 25 glucose (295 mOsm/kg). Slices  
435 were kept in room temperature ACSF until ready to measure and were used within 8 hours. All solutions  
436 were bubbled with carbogen (95% O<sub>2</sub>, 5% CO<sub>2</sub>) for the duration of the preparation and subsequent  
437 experiment.

438 For imaging, slices were mounted on Poly-L-Lysine (PLL) coated coverslips. Coverslips (Fisher  
439 #12-545-80) were plasma cleaned for 3 minutes, covered with 50-100  $\mu$ L 0.1% (w/v) PLL (150-300 kD)  
440 solution (Sigma #P8920) and allowed to dry under vacuum. Coverslips were thoroughly washed with  
441 nanopore water and dried before use. To mount the tissue, a slice was transferred to the PLL-coated  
442 face of the coverslip with a Pasteur pipette. Excess ACSF was pipetted or wicked away with filter paper,  
443 in the process flattening out the brain slice and adhering it to the glass. We found that this method  
444 worked reliably for coronal slices from one hemisphere but not for coronal slices from the entire brain.  
445 Coverslips were placed in a custom-built flow chamber with a microscope slide bottom and #1.5  
446 coverslip lid. ACSF was perfused at a rate of 1 mL/min with a VWR peristaltic pump.

447 The imaging protocol consisted of a 2 s imaging epoch followed by a 400 ms stimulation period  
448 and another 2 s imaging epoch. Each imaging epoch comprised 11 frames of functional Hadamard  
449 acquired with a 180 ms period under 100 mW/cm<sup>2</sup> 561 nm illumination. Blue light stimulation protocols  
450 are described in figure captions. The slice was allowed 6 s to recover before starting another imaging  
451 epoch. One run consisted of 6 imaging and stimulation rounds over one minute. Runs were repeated  
452 several times, spaced out by at least five minutes. NBQX and CPP, or TTX (Tocris) or retigabine,  
453 phenytoin, or carbamazepine (Sigma) were added to the ACSF from 1000x stock solutions after several  
454 baseline runs. In figure 4, brain slices were randomly selected from a pooled set of slices for different  
455 drug treatments.

456

#### 457 **Analysis of slice data.**

458 *Registration.* After reconstruction of Hadamard images (see Methods above), frames for each epoch  
459 were averaged together. Small movements and deformations in the slice over the course of multiple  
460 runs were corrected by automatic non-rigid registration (Klein et al., 2010). Functional Hadamard  
461 recording and structural Hadamard images were manually registered using a 2D affine transformation.

462

463 *Cell selection.*  $\Delta F$  images were calculated for each registered run by subtracting images acquired before  
464 blue light stimulation from images acquired immediately after blue light stimulation. Peaks in  $\Delta F$  images  
465 corresponded to individual cells, but noise in  $\Delta F$  varied as a result of brightness inhomogeneities in the  
466 slice, making it difficult to extract peaks directly. To correct for this noise, a widefield image for each  
467 slice was blurred with a 2D Gaussian with an 8 pixel (19.2  $\mu$ m) standard deviation, to remove nucleus  
468 sized objects. The square root of this image was used to normalize the  $\Delta F$  image of the slice. High spatial  
469 frequency noise was removed with a 2d Gaussian filter with a 0.5 pixel (1.2  $\mu$ m) standard deviation.  
470 Regions without expression were manually selected and standard deviations in these regions were  
471 chosen as a noise floor. Cells were identified as peaks in the normalized  $\Delta F$  image which had an  
472 amplitude larger than the noise floor by a user-defined factor, typically 7 – 10. Cells were required to  
473 have a minimum distance in space of 4 pixels (9.6  $\mu$ m) to avoid double counting cells. Once cell

474 locations were identified, single-cell fluorescence traces were extracted from corresponding locations in  
475 movies of unnormalized data blurred with 2d Gaussian filter with 1 pixel standard deviation.

476  
477 *Exclusion of spontaneously active and dying cells.* While measuring a large number of cells in an acute  
478 slice, a portion of cells showed spontaneous activity, characterized by transient fluorescent increases  
479 uncorrelated with blue light stimulation; and cell death, characterized by a large and irreversible  
480 increase in fluorescence. For **Figs. 6-9**, slices were imaged nine times, five times before AED application  
481 and four times after. Imaging epochs were averaged to generate movies with 108 frames (12 epochs per  
482 run x 9 runs). After extracting cell traces from these movies for all slices in the experiment, each cell's  
483 mean and standard deviation per run were calculated. Least squares fits on the mean and standard  
484 deviation were performed on 3-pre drug runs and projected to the full nine runs. Cells were excluded  
485 from further analysis if any projected mean or standard deviation was less than 1/15 of the cell's mean  
486 value or if the root mean square error of the fit was larger than 1/15 of the cell's mean value. This  
487 procedure rejected < 17% of cells.

488  
489 *Generation of excitability maps.* To generate the maps in **Fig. 7** the fluorescence trace for each included  
490 cell was normalized by subtracting its mean fluorescence values for each run and normalizing by the  
491 standard deviation for each run. For each cell, 3 pre-drug runs were averaged together to yield a 12  
492 element vector corresponding to normalized F in each epoch. Principal component analysis yielded 3  
493 main principal components which were then back-projected into pixel space for each slice, yielding the  
494 black and white images in **Fig. 7c**. Color images (**Fig. 7d,e**) were generated using L\*a\*b\* colorspace, by  
495 projecting PC1 into lightness, L, and PC2 and PC3 into the red-green and blue-yellow axes, a and b.

496 To generate maps of changes in drug response in **Fig. 8a**,  $\Delta F$  images from four runs before and  
497 after drug addition were averaged together, median filtered with a 3 pixel kernel, saturated at their  
498 99.5<sup>th</sup> percentile, and displayed in the green and red channels, respectively. The blue channel is the  
499 average of the red and green images. Color saturation was adjusted in L\*a\*b\* space to aid in  
500 visualization. In **Fig. 9**  $\Delta F$  images are scaled to the same absolute counts and shown in separate color  
501 channels.

502  
503 *Cortical layer analysis.* All striatal cells were pooled and treated separately. For cortical cells, cortex  
504 boundaries were manually defined in structural images as the surface of the brain and the bottom of  
505 Layer 6. Boundaries were registered to functional images (above) and cells were assigned a normalized  
506 depth coordinate based on these boundaries. Drug response, defined as  $\Delta F_{\text{drug}}/\Delta F_0$ , could then be  
507 related to normalized cortical depth. For each slice, cells were binned by cortical depth and the drug  
508 response per cell averaged over cells. Extreme cell responses were excluded from each bin using the  
509 generalized extreme Studentized deviate test. Layer boundary locations were taken from the primary  
510 somatosensory cortex in the matched coronal slices of the Allen Brain Reference Atlas.

511 KCNQ3 expression levels were acquired from Allen Brain Institute experiment #100041071. The  
512 somatosensory cortex was manually defined in 11 sagittal slices from a P28 male mouse. The available  
513 expression image was used to mask the raw data, but expression values were obtained directly from the  
514 raw ISH data. The edges of the cortex and cortical depth bins were defined as above and expression  
515 values were averaged together across slices from the same experiment.

516  
517 **Results**  
518 **A spectrally orthogonal Ca<sup>2+</sup> sensor and channelrhodopsin for 1-photon AON**  
519 AON requires a spectrally orthogonal optogenetic actuator and activity reporter (**Fig. 1a**). Examination of  
520 channelrhodopsin action spectra and Ca<sup>2+</sup> reporter excitation spectra suggested that the best approach

521 for 1-photon AON was to use a blue-shifted channelrhodopsin and a red-shifted genetically encoded  
522  $\text{Ca}^{2+}$  indicator (RGECI) (**Fig. 1a**). We thus set out to identify protein pairs suitable for this purpose.

523 We began by comparing the single action potential responses of RGECIs in cultured neurons.  
524 jRGECO1a was the most sensitive ( $\Delta F/F = 54 \pm 10\%$ ,  $n = \sim 120$  neurons). Unless otherwise indicated, all  
525 uncertainties are standard errors of the mean), followed by R-CaMP2 and jRCaMP1a, consistent with  
526 previous reports (**Fig. 1b, Table 1**) (Inoue et al., 2015). R-CaMP2 had the fastest kinetics ( $\tau_{\text{on}} = 26 \pm 10$   
527 ms,  $\tau_{\text{off}} = 270 \pm 20$  ms,  $n = \sim 120$  neurons), followed by jRGECO1a ( $\tau_{\text{on}} = 47 \pm 1$  ms,  $\tau_{\text{off}} = 440 \pm 40$  ms,  $n =$   
528  $\sim 120$  neurons) and jRCaMP1a (**Fig. 1c, Table 1**). In HEK293T cells, under basal  $\text{Ca}^{2+}$  conditions, jRGECO1a  
529 had the longest photobleaching time constant ( $\tau_{\text{bleach}} = 81 \pm 5$  s,  $I_{561} = 44 \text{ W/cm}^2$ ,  $n = 9$  cells), followed by  
530 R-CaMP2 and jRCaMP1a (**Table 1**). Under typical imaging conditions ( $I_{561} = 0.1 \text{ W/cm}^2$ ), photobleaching  
531 of jRGECO1a was thus < 10% during 1 hr of continuous imaging. While photobleaching is often a  
532 concern for 1P imaging, these results established that this effect was minor for wide-area imaging of  
533 jRGECO1a. We selected jRGECO1a for its superior sensitivity and photostability.

534 mApple-based fluorescent sensors, including jRGECO1a, are known to undergo photoswitching  
535 under blue light illumination (Akerboom et al., 2013; Dana et al., 2016). We thus sought a blue-shifted  
536 channelrhodopsin that could drive spikes in jRGECO1a-expressing neurons at blue intensities low  
537 enough to avoid optical crosstalk. TsChR is the most blue-shifted published ChR (**Fig. 1a**), but was  
538 initially reported to produce only  $\sim 40\%$  as much photocurrent as ChR2(H134R) (Klapoetke et al., 2014)  
539 and so has not previously been used in optogenetic applications. Addition of a  $K_{ir}2.1$  trafficking  
540 sequence (TS) and a GFP expression tag to TsChR led to excellent trafficking in cultured neurons (**Fig.**  
541 **1d**). We called this construct eTsChR-eGFP. Compared to ChR2(H134R), eTsChR had higher steady state  
542 photocurrents ( $470 \pm 42$  vs.  $288 \pm 60$  pA,  $p = 0.034$ , Student's *t*-test,  $n = 6$  neurons each, **Fig. 1e**). At the  
543 highest blue light intensity tested ( $33 \text{ W/cm}^2$ ), ChR2(H134R) passed a steady state photocurrent of  $288 \pm$   
544  $60$  pA; eTsChR passed the same steady state photocurrent at 100-fold lower intensity ( $0.33 \text{ W/cm}^2$ ).  
545 Compared to ChR2(H134R), eTsChR also had higher maximum steady state photocurrent densities ( $13.2 \pm$   
546  $1.2$  pA/pF vs.  $7.8 \pm 2.0$  pA/pF,  $p = 0.044$ , Student's *t*-test,  $n = 6$ ) and faster on- and off- kinetics (**Fig.**  
547 **1f,g**).

548 We co-expressed jRGECO1a and eTsChR in cultured rat hippocampal neurons, and used the far-  
549 red voltage-sensitive dye BeRST1 (Huang et al., 2015) as a ground-truth reporter of neural spiking.  
550 Flashes of blue light ( $0.7 \text{ W/cm}^2$ , 10 ms) induced action potentials, reported by BeRST1 fluorescence,  
551 and  $\text{Ca}^{2+}$  transients, reported simultaneously by jRGECO1a fluorescence (**Fig. 1h**). The sodium channel  
552 blocker TTX (1  $\mu\text{M}$ ) eliminated the light-evoked transients in both the BeRST1 and jRGECO1a  
553 fluorescence channels, confirming that the jRGECO1a response reflected spiking-dependent  $\text{Ca}^{2+}$  influx  
554 and that the optogenetic stimulation did not induce detectable photo-artifacts in the jRGECO1a  
555 fluorescence.

556 Cytoplasmic expression of jRGECO1a in brain slices led to a high level of fluorescence  
557 background from reporter present in neuropil, even with the optically sectioned imaging approaches  
558 described below (**Fig. 2a**). To facilitate imaging in tissue, we fused jRGECO1a to a Histone-2B (H2B) tag  
559 to localize expression to the nucleus (**Fig. 1d and Fig. 2b**), as previously done for zebrafish (Freeman et  
560 al., 2014) and rat (Skocek et al., 2018) brain imaging. The nuclear-localized H2B-jRGECO1a showed  
561 clearly resolved nuclei with little background between the cells. In cultured neurons, H2B-jRGECO1a  
562 responded to single action potentials with good sensitivity ( $\Delta F/F = 19.4 \pm 5.3\%$ ,  $n = 3$  cells), but with  
563 slower kinetics than the cytosolic reporter, ( $\tau_{\text{on}} = 167 \pm 27$  ms,  $\tau_{\text{off}} = 1,400 \pm 270$  ms) consistent with  
564 previous measurements of nuclear  $\text{Ca}^{2+}$  dynamics (**Fig. 2c**) (Eder and Bading, 2007; Bengtson et al.,  
565 2010).

566 We tested for optical crosstalk between actuator and reporter channels in cells co-expressing  
567 the optimized AON constructs. Due to the high sensitivity of eTsChR, the blue light doses needed to

568 elicit spikes ( $0.7 \text{ W/cm}^2$  for 10 ms,  $\lambda = 488 \text{ nm}$ ) induced minimal photoartifact in either cytoplasmic or  
569 nuclear jRGECO1a compared to a single-spike  $\text{Ca}^{2+}$  signal (-2% photoartifact in **Fig. 2d** vs. 19% spike  
570 response in **Fig. 1h**, **Fig. 2e**). Crosstalk from direct blue light excitation of jRGECO1a fluorescence was  
571 avoided in the experiments below by interleaved optogenetic stimulation and fluorescence imaging.

572 The yellow light used for  $\text{Ca}^{2+}$  imaging ( $\lambda = 561 \text{ nm}, 0.1 \text{ W/cm}^2$ ) induced in eTsChR a steady-state  
573 photocurrent less than 0.5 pA (**Fig. 2f**), far too small to trigger spurious action potentials. Expression of  
574 eTsChR did not significantly affect neurons' membrane resistance, membrane capacitance, or resting  
575 potential compared to controls (**Table 2**). Together, eTsChR and H2B-jRGECO1a formed a suitable  
576 actuator/reporter pair for crosstalk-free 1P AON.  
577

#### 578 **Hadamard microscopy enables optical sectioning in ultra-widefield images of acute brain slices**

579 We next sought to perform wide-area optically sectioned imaging of the AON constructs in acute brain  
580 slices. To achieve high light collection efficiency over a wide FOV, we designed a microscope system  
581 around a low magnification high numerical aperture objective (Olympus MVPLAPO 2 XC, NA 0.5). In  
582 wide-field epifluorescence mode, this microscope imaged a 4.6 mm FOV, large enough to capture most  
583 of a hemisphere of a coronal brain slice, with nominal  $2.25 \mu\text{m}$  lateral resolution set by the pixel size on  
584 the sCMOS detector. Apart from the optical filters and the mechanical mounts, all elements of the  
585 microscope were off-the-shelf components (**Methods**).

586 To achieve optical sectioning over a wide FOV, we developed a structured illumination approach  
587 based on Hadamard encoding. We placed a digital micromirror device (DMD) in the illumination path to  
588 enable arbitrary spatiotemporal patterning of the fluorescence excitation. Each DMD pixel mapped to  
589  $6.3 \mu\text{m}$  in the sample plane. The DMD modulated the excitation light with a series of binary illumination  
590 patterns such that neighboring sample locations were illuminated with orthogonal intensity sequences  
591 ( $P_1, P_2, \dots, P_n$  in **Fig. 3a**). Raw data consisted of a series of images ( $F(t_1), F(t_2), \dots, F(t_m)$  in **Fig. 3b-1**)  
592 acquired with each illumination pattern, which were then demodulated to yield images of the scattered  
593 light for each illumination location (**Fig. 3b-2**). Software binary masks then rejected scattered light (**Fig.**  
594 **3b-3**), akin to physical pinholes used in confocal microscopy. The sum of images over all illumination  
595 locations yielded an optical section (**Fig. 3b-4, Methods**). The Hadamard algorithm is linear and local,  
596 i.e. the image resulting from two distinct sources is the sum of the images of the individual sources; and  
597 the final intensity value at each pixel depends only on signals acquired at that pixel. Thus the results are  
598 independent of the sample and do not require any specialized post-processing.

599 To make all projected DMD pixels mutually orthogonal would require prohibitively long digital  
600 codes ( $\sim 10^6$  samples), but because light scatter is mostly local, repeating the codes periodically at  
601 separations larger than the scattering point-spread function resulted in minimal crosstalk (**Fig. 3c**).  
602 Residual crosstalk between repeated codes was scrambled by inverting the sequence of a randomly  
603 selected 50% subset of the pixels (**Fig. 3c, Methods**). This procedure resulted in series of patterns with  
604 50% duty cycle, uniform mean illumination across the sample, and uniform spatial and temporal spectral  
605 density. By varying the number of frames in the Hadamard sequence, one can systematically trade time  
606 resolution vs. background rejection. The workflow for acquiring and analyzing Hadamard images is  
607 summarized in **Fig. 3d**. A link to the software is given in **Methods**. Application of compressed sensing  
608 algorithms to Hadamard microscopy enabled signal extraction at half the frame rate of the camera  
609 (Parot et al., 2019) (**Fig. 10**), though this improved time resolution was not required for the applications  
610 described below.

611 We compared Hadamard microscopy to two other SIM techniques, stripe SIM (Gustafsson,  
612 2000) and HiLo (Mertz and Kim, 2010), all implemented using the same DMD and optics. Images of  $0.2 \mu\text{m}$   
613 fluorescent beads in agarose were used to estimate the point-spread functions (PSFs) of the three  
614 techniques in a non-scattering medium. As, expected, line sections through the three PSFs gave  
615 identical lateral (FWHM  $2.7 \mu\text{m}$ ) and axial (FWHM  $14.0 \mu\text{m}$ ) resolution near the focus (**Fig. 4**). For the

616 low-magnification, wide-area implementation described here, the resolution in all three cases was  
617 determined by the intersection of the pixel-size-limited DMD illumination spots and the camera  
618 collection PSFs. We performed optical simulations to explore whether lateral shifts between DMD pixels  
619 and the smaller camera pixels would lead to spatially varying spatial resolution. For the parameters of  
620 our experimental setup, the changes in spatial resolution were < 5% in lateral resolution and < 10% in  
621 axial resolution, so these effects were subsequently neglected.

622 The three imaging techniques differed critically in imaging parameters not captured by the  
623 FWHM of the PSFs, however. Stripe SIM and HiLo PSFs had out-of-focus conical lobes, a consequence of  
624 out-of-focus points emitting along the same rays as in-focus and laterally offset points. These lobes did  
625 not lie along either the lateral or axial line sections through the PSF, so they did not contribute to the  
626 PSF dimensions as usually characterized, but they contributed to substantial out-of-plane total  
627 fluorescence (**Fig. 4b**). Hadamard images lacked this artifact because use of multiple illumination  
628 patterns resolved ambiguities in assignment of out-of-focus fluorescence. For Hadamard microscopy,  
629 the integrated the PSF in the transverse (x-y) plane decayed to 15% of its peak at a defocus of -30  $\mu\text{m}$ ,  
630 whereas by the same measure HiLo retained 38% of peak fluorescence and stripe SIM retained 62% of  
631 peak fluorescence (**Fig. 4b**). Thus HiLo and stripe SIM suffered  $\sim$ 2.5-fold and  $\sim$ 4-fold higher background  
632 than Hadamard, respectively.

633 For the purpose of rejecting out-of-focus background fluorescence in tissue, the integrated  
634 transverse fluorescence, not the more commonly used axial line section, is the critical parameter. Thus  
635 we expected that Hadamard microscopy would perform better than stripe SIM or HiLo in resolving  
636 single-cell signals in densely expressing tissues. **Fig. 4c** and the **Discussion** compare the technical noise  
637 and shot noise properties of Hadamard and other SIM techniques. Hadamard performed as well as or  
638 better than the other techniques by these parameters.

639 We compared the performance of the three structured illumination techniques in brain tissue  
640 (**Fig. 5**). The sample comprised an acute 300  $\mu\text{m}$ -thick coronal brain slice, expressing nuclear-targeted  
641 jRGECO1a throughout cortex and striatum, and membrane-targeted ChRiff-GFP restricted by an Rbp4-  
642 Cre driver to a subset of Layer 5 (L5) pyramidal cells (**Fig. 5a**). Hadamard images clearly resolved  
643 individual cells, whereas wide-field epifluorescence did not (**Fig. 5b**). In the stripe SIM and HiLo images,  
644 out of focus nuclei appeared as bright rings, a consequence of the conical lobes on the PSF, which  
645 prevented clear separation of single-cell images (**Fig. 5c**). Light scattering caused the Hadamard signal to  
646 decay as a function of image depth with a length constant of 27  $\mu\text{m}$  in acute brain slices (**Fig. 5d,e**) and  
647 113  $\mu\text{m}$  in fixed slices. The difference in signal attenuation was attributed to decreased light scattering  
648 after the fixation process.

649 To quantify the ability of Hadamard microscopy to resolve single-cell signals, we used high-  
650 resolution confocal microscopy to make ground-truth maps of the spatial distribution of nuclei in fixed  
651 slices densely expressing nuclear jRGECO1a. We then simulated Hadamard images of these cells in  
652 scattering tissue and estimated the crosstalk, i.e. the spurious contribution from all other cells to the  
653 fluorescence signal ascribed to each nucleus (Methods). In cortical layer 2/3, only 10% of the cells  
654 received more than 20% crosstalk from other cells. The crosstalk was lower in other brain regions (**Fig.**  
655 **5f**). Cell nuclei had a stereotyped round and localized shape. The degree of crosstalk could be estimated  
656 on a cell-by-cell basis via shape deviations. If desired, cells with crosstalk beyond a threshold value  
657 could be discarded from the analysis, though this procedure was not used here. Hadamard microscopy  
658 thus enabled optically sectioned imaging with single-cell resolution over wide fields of view in acute  
659 brain slices.

660

#### 661 **Mapping excitability in acute slices**

662 To map neural excitability, we applied Hadamard microscopy with simultaneous optogenetic stimulation  
663 in acute mouse brain slices expressing the actuator-reporter pair. We co-injected AAV9-hSyn-DO-H2B-

664 jRGECO1a and AAV9-hSyn-eTsChR in cortex and striatum of wild-type P0-2 mouse neonates (**Fig. 6a**).  
665 Both proteins expressed well and were readily visualized via Hadamard imaging in 300  $\mu$ m acute brain  
666 slices from 3-week-old animals (**Fig. 6b,c**). We performed Hadamard AON measurements in a region 2.3  
667  $\times$  2.3 mm, set by the size of the expressing region. Cell signals were acquired from a depth of 32  $\pm$   
668 13  $\mu$ m (**Fig. 5d**).

669 To probe excitability, we exposed the slice to a series of wide-field blue stimuli of increasing  
670 strength, interleaved with Hadamard imaging of H2B-jRGECO1a with yellow light (561 nm, 100 mW/cm<sup>2</sup>,  
671 **Fig. 6d**). Hadamard images were first acquired for 2 s to establish baseline fluorescence. Then a brief  
672 burst of blue light pulses (470 nm, 8 pulses, 15 mW/cm<sup>2</sup>, 5 ms duration, 20 Hz) evoked neural activity,  
673 followed by another 2 s of Hadamard imaging to record the response. This image-stimulate-image  
674 procedure was repeated at 10 s intervals, six times, with the intensity of the blue light doubling upon  
675 each repetition to a maximum of 480 mW/cm<sup>2</sup>. This measurement protocol reported the changes in  
676 intracellular Ca<sup>2+</sup> concentration as a function of optogenetic stimulus strength.

677 Neighboring cells often showed distinct patterns of Ca<sup>2+</sup> dynamics, while interstitial regions  
678 showed undetectable fluorescence (**Fig. 6d,e**), confirming that Hadamard microscopy effectively  
679 rejected scatter and out-of-focus background. The yellow light used for Ca<sup>2+</sup> imaging induced spurious  
680 activity in only 0.46  $\pm$  0.03% of cells ( $n = 38,835$  cells, 9 slices), establishing that the imaging light only  
681 weakly activated eTsChR. The sodium channel blocker tetrodotoxin (TTX, 1  $\mu$ M) abolished blue light  
682 evoked responses slice wide, confirming that Ca<sup>2+</sup> responses were due to action potential firing (**Fig.**  
683 **6f,g**) and, furthermore, that blue light-induced photoswitching was minimal.

684 We tested the long-term stability of the preparation. The optogenetically induced Ca<sup>2+</sup> signal  
685 was stable over a 78 minute session comprising 7 repeated imaging cycles (**Fig. 6h,i**). During this period  
686 the population-average optically evoked  $\Delta F/F$  at the strongest stimulus decreased modestly from 64  $\pm$   
687 0.7% to 52  $\pm$  0.7%,  $n = 3,195$  cells. These results demonstrate the capability for repeated measurements  
688 over > 1 h in a single sample.

689 We used a 2D peak-finding algorithm to identify  $n = 6,102$  responding cells in the Hadamard  
690 images of a single brain slice (**Fig. 7a**). Cells showed different patterns of response in the striatum vs.  
691 cortex, but we also observed cell-to-cell variability within the cortex. To characterize this variability, we  
692 applied principal components analysis (PCA) to a set of single-cell recordings. First, we repeated the  
693 excitability measurement on 9 slices from 2 animals, recording from a total of  $n = 32,103$  cells across  
694 cortex and striatum. Measurement runs (comprising six measure-stimulate-measure sequences) were  
695 repeated at 5-minute intervals, 3 times per slice. PCA identified 3 main temporal components in the  
696 single-cell fluorescence responses (**Fig. 7b,c, Methods**). Examination of the PC temporal waveforms  
697 showed that PC1 measured overall fluorescence response amplitude, PC2 captured a left-right shift in  
698 the sigmoidal excitability profile, and PC3 largely captured a stimulus-dependent increase in baseline  
699 fluorescence.

700 We then decomposed the fluorescence waveform at each pixel into its principal components  
701 (PCs), and color-coded each pixel by its PC amplitudes (**Fig. 7d,e, Methods**). Despite coloring each pixel  
702 independently, individual cells appeared homogeneously colored in the resulting image (**Fig. 7e**),  
703 consistent with the low cell-to-cell fluorescence crosstalk. These maps revealed striking colored bands  
704 running along the cortical layers, demonstrating different functional responses in different brain regions.  
705 Intriguingly, some layers appeared relatively homogeneous (L2/3, L4, L6), while cells in L5 had larger  
706 cell-to-cell variations in response. These results demonstrate that Hadamard AON can map excitability  
707 over thousands of individual neurons across large areas of acute brain slice.

#### 708 709 **Mapping pharmacological responses with Hadamard AON**

710 Wide-area AON offers a means to map the cell type and region-specific effects of pharmacological or  
711 other perturbations on neural excitability. We performed excitability measurements on acute slices

712 before and after applying the antiepileptic drugs (AEDs) retigabine (25  $\mu$ M), carbamazepine (100  $\mu$ M),  
713 and phenytoin (100  $\mu$ M). To quantify the drug effect, we measured the pixel-by-pixel change in mean  
714 amplitude,  $\Delta F$ , of the optogenetically induced response—a parameter close to the first principal  
715 component that emerged from the unsupervised analysis above. Each drug had different effects in  
716 striatum and cortex, and attenuated cortical excitability in a distinctive spatial pattern (**Fig. 8a**).

717 We sorted cells into bins based on their cortical depth and visualized mean AED response as a  
718 function of cortical depth, averaged over  $n = 3$  slices per drug (**Fig. 8b**). Carbamazepine and phenytoin,  
719 both sodium channel blockers, showed relatively uniform suppression of excitability as a function of  
720 cortical depth, but retigabine showed a graded response, weakest in L6b and strongest in L4.

721 Retigabine is a specific positive allosteric modulator of K<sub>v</sub>7 channels, and its primary target is  
722 thought to be the K<sub>v</sub>7.2/7.3 heteromer (Gunthorpe et al., 2012), coded for by the genes KCNQ2 and  
723 KCNQ3. We examined the Allen Brain Atlas map of the expression level of KCNQ3 (Lein et al., 2007), as  
724 determined by RNA *in situ* hybridization (ISH), and found statistically significant correlation between  
725 KCNQ3 expression level and effect of retigabine (Pearson's  $r = -0.40$ , 95% confidence interval between -  
726 0.022 and -0.69 obtained by bootstrapping, **Fig. 8c-d**). Higher expression of KCNQ3 correlated with  
727 greater inhibition of excitability by retigabine, as one would expect for a potassium channel activator. An  
728 independent ISH study in adult animals reported a similar distribution of KCNQ2 and KCNQ3 (Saganich et  
729 al., 2001). These results establish a connection between the Hadamard AON measurements and the  
730 underlying pattern of ion channels.

731

### 732 **Probing functional connectivity with ultra-widefield AON**

733 We next sought to extend the Hadamard AON platform to measurements of functional connectivity.  
734 Although slicing interrupts many long-range projections, optogenetic stimulation of axon terminals can  
735 nonetheless evoke local neurotransmitter release and postsynaptic responses (Petreanu et al., 2007).  
736 We reasoned that sufficiently strong presynaptic stimulation would drive postsynaptic spikes, which  
737 could be detected via H2B-jRGECO1a.

738 To achieve this goal, the channelrhodopsin must traffic efficiently to axon terminals. We found  
739 that expression of eTsChR was predominantly localized to the soma and dendrites (**Fig. 9a**). We thus  
740 explored CheRiff-TS-GFP (CheRiff), a blue-light sensitive, high-photocurrent channelrhodopsin  
741 (Hochbaum et al., 2014). CheRiff trafficked well in axons (**Fig. 9b,c**) and was 2.3-fold more sensitive to  
742 blue light than eTsChR. CheRiff was also more sensitive to yellow light, raising the possibility of spurious  
743 activation by the 561 nm imaging laser. Under typical imaging conditions (561 nm, 100 mW/cm<sup>2</sup>)  
744 CheRiff photocurrent was 0.9% of the maximum photocurrent (95% confidence interval 0.8 to 1%,  $n = 7$   
745 cells, **Fig. 9d**), whereas eTsChR photocurrent was < 0.1% of its maximum photocurrent (**Fig. 2f**).

746 We designed an experiment to express CheRiff in L5 cortico-striatal neurons following a  
747 previously described protocol (Ibrahim et al., 2016; Wu et al., 2015), and to test the postsynaptic  
748 response via Ca<sup>2+</sup> imaging in the striatum. The CheRiff vector comprised CAG-DIO-CheRiff-TS-GFP (Cre-  
749 on CheRiff), which we injected into neonatal Rbp4-Cre<sup>+/−</sup> mice to target expression to a population of  
750 excitatory L5 neurons. We concurrently injected hSyn-DO-H2B-jRGECO1a (Cre-off nuclear Ca<sup>2+</sup> indicator)  
751 to drive reporter expression throughout striatum and cortex (**Fig. 9e**).

752 First, we tested the slices for spurious activity elicited by the yellow imaging light. Very few  
753 striatal neurons showed a detectable increase in H2B-jRGECO1a signal caused by 561 nm imaging  
754 illumination ( $0.32 \pm 0.001\%$ ,  $n = 3137$  cells, 2 slices, **Fig. 9f,g**), confirming that the yellow light did not  
755 excite axon terminals enough to drive postsynaptic spikes in most cases. This crosstalk performance is  
756 not significantly different from that in the eTsChR-based excitability measurements described above  
757 ( $0.46 \pm 0.03\%$ ,  $n = 38,835$  cells, 9 slices,  $p = 0.25$ , two-proportion z-test, **Fig. 9h**). In excitability-style  
758 measurements with CheRiff, a significantly larger proportion of neurons showed imaging light-induced  
759 activation ( $2.3 \pm 0.5\%$ ,  $n = 944$  cells, 2 slices,  $p = 8 \times 10^{-10}$ ). Thus, the superior axonal trafficking of CheRiff

760 made it the preferred actuator for functional connectivity measurements, while the lower yellow-light  
761 crosstalk of eTsChR made it the preferred actuator for excitability measurements.

762 We then repeated the blue-light stimulation and imaging protocol previously used for  
763 excitability measurements while monitoring downstream responses in the striatum. Blue light induced  
764 nuclear  $\text{Ca}^{2+}$  transients across the cortex and striatum (**Fig. 9i**). Blockers of excitatory transmission, NBQX  
765 and CPP, reversibly eliminated the responses in the striatum, Layer 6, and Layer 2/3, confirming that  
766 these responses were synaptically evoked (**Fig. 9i**) and that there was negligible blue light crosstalk into  
767 the fluorescence signals.

768 To our surprise, addition of NBQX and CPP reversibly increased the optogenetically induced  
769 activity in a population of cells in L5 (**Fig. 9j,k**). These cells showed little or no response to stimulation  
770 prior to addition of synaptic blockers (**Fig. 9k**). The location of these cells amidst the Rbp4 population  
771 suggested that these cells expressed both the actuator and reporter (likely a consequence of imperfect  
772 silencing of DO-H2B-jRGECO1a in Rbp4-Cre<sup>+</sup> neurons (Saunders et al., 2012)). The increase in excitability  
773 upon excitatory blockade then implies a disinhibitory mechanism, i.e. that these L5 cells received  
774 disynaptic inhibition from Rbp4-Cre labeled L5 pyramidal cells, which was relieved under excitatory  
775 blockade. The remaining cells in L5 showed a reversible decrease of activity in the presence of excitatory  
776 synaptic blockers, similar to the phenotypes in striatum and other cortical layers. These intermixed  
777 responses highlight the importance of performing single cell resolution measurements with Hadamard  
778 microscopy. Further, although Hadamard microscopy of jRGECO1a can only study supra-threshold  
779 responses, these results shown that judicious pharmacological applications can dissect a system's  
780 functional connectivity.  
781

#### 782 **High-speed Hadamard AON with compressed sensing**

783 Finally, we illustrate that Hadamard AON can be performed at high speed by using recently developed  
784 compressed sensing techniques (Parot et al., 2019). The core idea is to take advantage of the low-rank  
785 dynamics of fluorescence fluctuations in neuronal samples. Since each neuron covers multiple camera  
786 pixels, every image has redundant information. In the context of a sufficiently long recording, a pair of  
787 images comprising a single Hadamard pattern and its complement contain enough information to infer  
788 the images that would have been recorded under illumination with any other Hadamard pattern. By  
789 inferring the complete set of Hadamard images for every pair of camera frames, this approach enables  
790 optically sectioned reconstructions at half of the camera frame-rate. **Fig. 10** illustrates this approach.  
791 The sample comprised a hippocampal slice co-expressing eTsChR and nuclear-localized jRGECO1a. To  
792 ensure that each nucleus was illuminated by multiple DMD pixels, we used a 10x objective (**Methods**).  
793 The optogenetic stimulation was as in **Figs. 6** and **7**. The camera and DMD-patterned illumination were  
794 synchronized to run at 66 Hz.  
795

796 **Fig. 10a** shows a Hadamard image of the whole field of view, in which nuclei have been color-  
797 coded by the principal component amplitudes of their dynamic response, as in **Fig. 7d**. A close-up image  
798 (**Fig. 10b**) shows the individually resolved nuclei. A wide-field image sequence was calculated by  
799 averaging together pairs of frames with complementary illumination patterns. Hadamard  
800 reconstructions were calculated via the standard approach outlined above, and via the compressed  
801 sensing approach.

802 Regions 1 and 5 in **Fig. 10a** corresponded to a cell-free interstitial region and a non-responsive  
803 (presumably dead) very bright cell, respectively, whereas regions 2 – 4 corresponded to optogenetically  
804 responsive cells. **Fig. 10b** shows that the wide-field images had high time resolution, but suffered from  
805 out-of-focus crosstalk: the gray traces from regions 1 and 5 showed spurious optogenetically induced  
806 responses. In the conventional Hadamard movie, the intensity traces from regions 1 and 5 showed  
807 constant fluorescence, confirming effective background rejection. But these extracted traces had low  
808 time resolution. In the compressed sensing Hadamard movie, the intensity traces from regions 1 and 5

808 had the same time resolution as in the wide-field movie (33 Hz), but lacked background crosstalk as in  
809 the conventional Hadamard movie. Thus compressed Hadamard imaging provides a means to achieve  
810 simultaneously optical sectioning and high time resolution.

811

## 812 Discussion

813 Through detailed photophysical characterization of optogenetic actuators and reporters, we identified  
814 pairs that can be used in tandem with minimal 1P crosstalk. A pairing of CheRiff and jRCaMP1b was  
815 recently demonstrated in cultured neurons, but crosstalk was not measured quantitatively and the  
816 genetic constructs were not tested in tissue (Afshar Saber et al., 2018). Despite the well reported  
817 photophysical blue light artifacts in jRGECO1a, we found that sufficiently sensitive optogenetic actuators  
818 could induce neuronal responses at blue light intensities where these artifacts were minimal. The far  
819 blue-shifted channelrhodopsin, eTsChR, enabled measurements of intrinsic excitability, and the highly  
820 sensitive channelrhodopsin, CheRiff, enabled measurements of functional connectivity, in both cases  
821 with minimal crosstalk from the yellow imaging laser. Finally, nuclear localization of the reporter,  
822 combined with Hadamard structured illumination microscopy enabled resolution of single-cell signals  
823 across wide areas of brain slice. The resulting toolbox is well suited for studying suprathreshold  
824 phenotypes in acute brain slice, such as excitability of single neurons and functional connectivity of  
825 strong excitatory connections. These tools enable wide-area mapping of these properties in brain tissue,  
826 and studies on the effects of perturbations thereon.

827 Questions of where and how neuroactive compounds affect neuronal function are difficult to  
828 answer with conventional techniques. Typically, compound distribution is investigated by radiographic  
829 labeling experiments. Such results are convolved with possible nonspecific binding of the molecule and  
830 with expression of the target in the neuropil, preventing single cell identification. The 1P AON technique  
831 provides a high spatial resolution functional alternative to radiographic mapping. We show differential  
832 response profiles for three AEDs—one molecularly specific drug, retigabine, whose response profile  
833 matched its known target distribution, and two non-specific drugs, carbamazepine and phenytoin.  
834 Measurements on other drugs may provide insights into their specific cellular and regional targets.  
835 Hadamard AON could also be used to probe the effects of neuropeptides, neuromodulators, hormones,  
836 genetic mutations, or environmental perturbations (e.g. temperature, oxygen, metabolites) on brain-  
837 wide patterns of neural excitability.

838 By extending these assays to measurements of functional connectivity, we show that this 1P  
839 AON toolbox can be also be used for circuit dissection. The all-optical connectivity assay of Figure 9  
840 shows that Rbp4-Cre positive neurons have a strong excitatory drive across striatum, consistent with  
841 previous results (Kozorovitskiy et al., 2015). The net effect of layer 5 stimulation on other cortical layers  
842 was not previously well established—most L5 neurons are excitatory but also recruit strong inhibition  
843 via parvalbumin and somatostatin neurons across the cortical column (Jiang et al., 2015; Naka and  
844 Adesnik, 2016). We found a clear net excitatory effect of Rbp4-Cre neuron activation in many cells of  
845 L2/3 and L6a of the cortex. Within L5 we found a heterogeneous response, where inhibition outweighed  
846 excitation in Rbp4-cre positive neurons (and possibly others which remained nonresponsive during the  
847 entire experiment) but excitation outweighed inhibition in other neurons in L5. While this paper was in  
848 review, another study interrogated the same circuit with optogenetic stimulation and simultaneous  
849 triple whole cell patch clamp, with broadly similar conclusions (Adesnik, 2018), though the difficulty of  
850 patch clamp limited the measurements to a few tens of neurons overall.

851 Both 1P AON and Hadamard microscopy can be used independently and neither technique is  
852 limited to neuroscience applications. The far blue spectrum and excellent sensitivity of eTSChR open the  
853 possibility to pair it with red-shifted fluorescent sensors of many other modalities, such as pH, cyclic  
854 AMP, or neurotransmitters. The broad spectral range of Hadamard microscopy opens possibilities for

855 high-speed optically sectioned imaging of many different fluorescent reporters, including simultaneous  
856 imaging of multiple modalities.

857 There are many microscopy techniques which could in principle be used for AON in brain slices.  
858 Here we briefly outline the factors which led us to develop Hadamard microscopy rather than using an  
859 established technique. Spinning disk confocal microscopy (Toomre et al., ) in principle provides high  
860 temporal resolution and good optical sectioning, but existing spinning disk optics lack sufficient etendue  
861 to capture the FOV and NA of the wide-area objective. One could mimic the function of a spinning disk  
862 system by activating individual DMD pixels sequentially in a tiled array, acquiring one image per  
863 illumination pattern, and then using software spatial filtering to keep only the in-focus component of  
864 each point illumination pattern. This approach would yield the same PSF as Hadamard microscopy.

865 Unmixing techniques such as Hadamard microscopy cannot unmix shot noise. Here we compare  
866 the shot noise properties of the Hadamard images relative to DMD-based multi-focal confocal. Let  $S$  be  
867 the mean number of signal photons acquired in one camera pixel in one frame when the corresponding  
868 DMD pixel is turned on. Let  $\alpha$  be the mean number of background photons acquired in camera pixel  $i$  in  
869 one frame when DMD pixel  $j \neq i$  is turned on, averaged over all  $j$  within a block of  $N$  pixels. A simple  
870 analysis of the shot noise implies that in multi-focal confocal (i.e. one DMD pixel turned on at a time) the  
871 shot noise-limited signal-to-noise ratio is  $SNR = \sqrt{S}$ . A short calculation shows that in Hadamard  
872 microscopy, the shot noise-limited SNR is approximately:

$$873 SNR = \frac{S}{\sqrt{2\alpha}}$$

874 If  $\alpha < S/2$ , then Hadamard is better; otherwise multi-focal confocal is better. We found experimentally  
875 that for  $N = 12$ ,  $\alpha/S = 0.51$ , indicating comparable shot noise for the multi-focal and Hadamard  
876 approaches. For  $N = 64$ , we measured  $\alpha/S = 0.26$ , indicating superior performance of Hadamard over  
877 multi-focal confocal. In these comparisons, the total optical dose into the sample is greater for  
878 Hadamard than for multifocal. The duty cycle of illumination is  $1/N$  for multifocal confocal, and  $1/2$  for  
879 Hadamard, so for  $N = 12$ , Hadamard exposes the sample to 6-fold more light, and for  $N = 64$ , Hadamard  
880 uses 32-fold more light. While photobleaching and phototoxicity were not significant factors in the  
881 present experiments, the presence of these effects may favor multifocal confocal.

882 As discussed above, stripe SIM and HiLo techniques are alternatives which could be  
883 implemented with the same DMD optics as Hadamard microscopy. The improved PSF shape (relative to  
884 stripe SIM and HiLo) and the absence of static illumination noise (relative to HiLo) favored Hadamard  
885 microscopy. The contributions of background photons to the shot noise are identical in all three  
886 techniques. The lower temporal resolution of Hadamard relative to the other SIM techniques did not  
887 constrain the ability to map nuclear  $Ca^{2+}$  dynamics, though better time resolution may be needed for  
888 other fluorescent reporters. Improvement in the time resolution of Hadamard microscopy are possible  
889 via compressed sensing techniques (Parot et al., 2019).

890 2P mesoscopes currently hold the record for most single neurons ( $\sim 3000$ ) recorded  
891 simultaneously in tissue (Sofroniew et al., 2016). 2P-mesoscopes have greater depth penetration than  
892 SIM techniques, making them more suitable for *in vivo* studies at present. Point-scanning based  
893 mesoscopes have achieved pixel rates of  $\sim 2 \times 10^7$ /s over  $0.6 \times 0.6$  mm FOVs but the requirement to  
894 translate the beam long distances limits pixel rates over large FOVs ( $4.4 \times 4.2$  mm) to  $5.6 \times 10^6$ /s.  
895 Acousto-optical steering allows fast 2P random-access imaging (Szalay et al., 2016), but this technique  
896 has only been demonstrated in a FOV of 0.5 mm, limited by the etendue of the acousto-optical  
897 deflectors. With 12-pattern Hadamard, we achieved comparable data rates of  $1.2 \times 10^7$ /s over a  $4.6 \times$   
898  $2.3$  mm FOV, with optically sectioned single-cell resolution. With improved control software to  
899 synchronize Hadamard patterns to the rolling shutter of the camera, pixel rates of  $3.3 \times 10^7$  pixels/s over  
900 the entire  $4.6 \times 4.6$  mm FOV would be possible with current camera technology. Finally, in contrast to

901 2P-mesoscopes, Hadamard microscopy is readily implemented with inexpensive LED or diode laser  
902 illumination across a broad range of excitation wavelengths.

903 Even when imaging in acute slices, one must achieve sufficient depth penetration to avoid  
904 damaged cells near the surface. Due to the great effort and low throughput of manual patch clamp  
905 measurements, it is typical to record at a depth of 50  $\mu\text{m}$  or greater to minimize the risk of patching an  
906 unhealthy cell, though recent protocols suggest 30  $\mu\text{m}$  is sufficient (Ting et al., 2018). Our approach  
907 includes procedures to identify and exclude dead (non-responsive) cells. Hadamard AON measures large  
908 enough numbers of cells that one can afford to discard a few unhealthy cells, while still maintaining  
909 excellent statistics. The stable excitability and anticipated responses to tool pharmacology (Fig. 6)  
910 establish that the cells assayed in our methods are adequately healthy from a functional perspective,  
911 despite being only  $\sim$ 30  $\mu\text{m}$  below the surface.

912 For precisely targeted single-cell stimulation, 2P optics are essential, but for wide-area  
913 optogenetic stimulation, 1P optics are preferable, as follows: 2P optogenetic stimulation requires time-  
914 average optical powers of 20 – 80 mW/cell (Shemesh et al., 2017; Ronzitti et al., 2017; Mardinly et al.,  
915 2018). Maximal safe steady-state 2P optical power into intact brain tissue is  $\sim$ 200 mW (Podgorski and  
916 Ranganathan, 2016), limiting simultaneous 2P stimulation to at most a few tens of neurons at a time. 1P  
917 optogenetic stimulation requires approximately  $10^6$ -fold lower time-average power ( $\sim$ 50 nW/cell)  
918 (Hochbaum et al., 2014), and thus is readily applied over wide areas of tissue to many thousands of cells  
919 simultaneously.

920 If a microscope can measure  $N$  cells in parallel, a measurement protocol takes time  $\tau$ , and an  
921 acute slice is viable for time  $T$ , then the total number of cells that can be measured is  $NT/\tau$ . A typical  
922 excitability measurement (including focusing and saving data) takes  $\tau \sim 2$  min. In the present work, the  
923 field of view was limited by the range of viral gene expression, but in transgenic animals or with recently  
924 developed systemic gene delivery techniques (Chan et al., 2017), functional measurements could be  
925 made across an entire brain slice. With the current FOV, Hadamard microscopy could tile a complete  
926 sagittal slice in 7 acquisitions, or  $\sim$ 14 min. Brain slices typically remain viable for  $T \sim 5$  hrs. Thus one  
927 could record from  $\sim$ 20 slices, enough to create a brain-wide functional map. Such a mapping technique  
928 could provide an unbiased approach to studying neuronal excitability, functional connectivity, and  
929 pharmacology across an entire brain.

930

### 931 Acknowledgments

932 We thank Vaibhav Joshi, Katherine Williams, and Melinda Lee for technical assistance. We thank  
933 Bernardo Sabatini for Rbp4-Cre mice, and Christopher Werley for assistance with the microscope design.  
934 We thank Daryl Lim for providing HiLo reconstruction code. Joshua Sanes provided support for the  
935 cloning of H2B-jRGECO1a. This work was supported by the Howard Hughes Medical Institute. SLF was  
936 supported by an NSF Graduate Research Fellowship. VJP was supported by a Becas Chile scholarship.  
937 Work in David Cox's lab was supported by IARPA (contract #D16PC00002) and the Mind Brain Behavior  
938 Faculty Award of Harvard.

### 939 Author contributions

940 SLF designed, created, and calibrated the optogenetic constructs. VJP designed and built the Hadamard  
941 microscope with early assistance from JJK. AG and MY cloned H2B-jRGECO1a and characterized its  
942 response via patch clamp electrophysiology. AA cloned eTsChR. YA helped with brain slice work. SL  
943 provided brain slices broadly expressing fluorescent proteins. REC supervised the contribution from AA.  
944 DDC supervised the contribution from AG. AEC conceived the Hadamard microscopy concept and

945 supervised the research. SLF and VJP acquired data. SLF, VJP, and AEC analyzed data. SLF, VJP, and AEC  
946 wrote the paper.

947

948 **Data and code availability**

949 Constructs will be made available on Addgene. Code for Hadamard pattern generation and image  
950 reconstruction, as well as raw data examples are linked in the Methods section.

951 **Competing financial interests**

952 AEC and VJP have filed a patent application on Hadamard microscopy. AEC is a co-founder of Q-State  
953 Biosciences.

954 **References**

955 Adesnik H (2018) Layer-specific excitation/inhibition balances during neuronal synchronization in the

956 visual cortex. *J Physiol (Lond)* 596:1639-1657.

957 Afshar Saber W, Gasparoli FM, Dirks MG, Gunn-Moore FJ, Antkowiak M (2018) All-optical assay to study  
958 biological neural networks. *Frontiers in Neuroscience* 12:451.

959 Akerboom J *et al.* (2013) Genetically encoded calcium indicators for multi-color neural activity imaging  
960 and combination with optogenetics. *Front Mol Neurosci* 6:2.

961 Bengtson CP, Freitag HE, Weislogel JM, Bading H (2010) Nuclear calcium sensors reveal that repetition of  
962 trains of synaptic stimuli boosts nuclear calcium signaling in CA1 pyramidal neurons. *Biophys J* 99:4066-  
963 4077.

964 Blot A, Barbour B (2014) Ultra-rapid axon-axon ephaptic inhibition of cerebellar purkinje cells by the  
965 pinceau. *Nat Neurosci* 17:289.

966 Carrillo-Reid L, Yang W, Bando Y, Peterka DS, Yuste R (2016) Imprinting and recalling cortical ensembles.  
967 *Science* 353:691-694.

968 Chan KY, Jang MJ, Yoo BB, Greenbaum A, Ravi N, Wu WL, Sanchez-Guardado L, Lois C, Mazmanian SK,  
969 Deverman BE, Grdinaru V (2017) Engineered AAVs for efficient noninvasive gene delivery to the central  
970 and peripheral nervous systems. *Nat Neurosci* 20:1172-1179.

971 Chen T, Wardill TJ, Sun Y, Pulver SR, Renninger SL, Baohan A, Schreiter ER, Kerr Ra, Orger MB, Jayaraman  
972 V, Looger LL, Svoboda K, Kim DS (2013) Ultrasensitive fluorescent proteins for imaging neuronal activity.  
973 499:295-300.

974 Dana H, Mohar B, Sun Y, Narayan S, Gordus A, Hasseman JP, Tsegaye G, Holt GT, Hu A, Walpita D, Patel  
975 R, Macklin JJ, Bargmann CI, Ahrens MB, Schreiter ER, Jayaraman V, Looger LL, Svoboda K, Kim DS (2016)  
976 Sensitive red protein calcium indicators for imaging neural activity. *eLife* 5:10.7554/eLife.12727.

977 Eder A, Bading H (2007) Calcium signals can freely cross the nuclear envelope in hippocampal neurons:  
978 Somatic calcium increases generate nuclear calcium transients. *BMC Neurosci* 8:57.

- 979 Emiliiani V, Cohen AE, Deisseroth K, Haussser M (2015) All-optical interrogation of neural circuits. *J  
980 Neurosci* 35:13917-13926.
- 981 Freeman J, Vladimirov N, Kawashima T, Mu Y, Sofroniew NJ, Bennett DV, Rosen J, Yang CT, Looger LL,  
982 Ahrens MB (2014) Mapping brain activity at scale with cluster computing. *Nat Methods* 11:941-950.
- 983 Gunthorpe MJ, Large CH, Sankar R (2012) The mechanism of action of retigabine (ezogabine), a first-in-  
984 class K<sup>+</sup> channel opener for the treatment of epilepsy. *Epilepsia* 53:412-424.
- 985 Gustafsson MG (2000) Surpassing the lateral resolution limit by a factor of two using structured  
986 illumination microscopy. *J Microsc* 198:82-87.
- 987 Harnett MT, Xu N, Magee JC, Williams SR (2013) Potassium channels control the interaction between  
988 active dendritic integration compartments in layer 5 cortical pyramidal neurons. *Neuron* 79:516-529.
- 989 Hochbaum DR *et al.* (2014) All-optical electrophysiology in mammalian neurons using engineered  
990 microbial rhodopsins. *Nat Methods* 11:825-833.
- 991 Huang YL, Walker AS, Miller EW (2015) A photostable silicon rhodamine platform for optical voltage  
992 sensing. *J Am Chem Soc* 137:10767-10776.
- 993 Ibrahim LA, Mesik L, Ji XY, Fang Q, Li HF, Li YT, Zingg B, Zhang LI, Tao HW (2016) Cross-modality  
994 sharpening of visual cortical processing through layer-1-mediated inhibition and disinhibition. *Neuron*  
995 89:1031-1045.
- 996 Inoue M, Takeuchi A, Horigane S, Ohkura M, Gengyo-Ando K, Fujii H, Kamijo S, Takemoto-Kimura S, Kano  
997 M, Nakai J (2015) Rational design of a high-affinity, fast, red calcium indicator R-CaMP2. *Nature Methods*  
998 12:64-70.
- 999 Jiang X, Shen S, Cadwell CR, Berens P, Sinz F, Ecker AS, Patel S, Tolias AS (2015) Principles of connectivity  
1000 among morphologically defined cell types in adult neocortex. *Science* 350:aac9462.
- 1001 Klapoetke NC, Murata Y, Kim SS, Pulver SR, Birdsey-Benson A, Cho YK, Morimoto TK, Chuong AS,  
1002 Carpenter EJ, Tian Z (2014) Independent optical excitation of distinct neural populations. *Nat Meth*  
1003 11:338-346.
- 1004 Klein S, Staring M, Murphy K, Viergever MA, Pluim JP (2010) Elastix: A toolbox for intensity-based  
1005 medical image registration. *IEEE Trans Med Imaging* 29:196-205.
- 1006 Kozorovitskiy Y, Peixoto R, Wang W, Saunders A, Sabatini BL (2015) Neuromodulation of excitatory  
1007 synaptogenesis in striatal development. *Elife* 4:e10111.
- 1008 Lein ES, Hawrylycz MJ, Ao N, Ayres M, Bensinger A, Bernard A, Boe AF, Boguski MS, Brockway KS, Byrnes  
1009 EJ (2007) Genome-wide atlas of gene expression in the adult mouse brain. *Nature* 445:168.
- 1010 Mardinly AR, Oldenburg IA, Pegard NC, Sridharan S, Lyall EH, Chesnov K, Brohawn SG, Waller L, Adesnik  
1011 H (2018) Precise multimodal optical control of neural ensemble activity. *Nat Neurosci* 21:881-893.
- 1012 Mazzaferri J, Kunik D, Belisle J, Singh K, Lefrançois S, Costantino S (2011) Analyzing speckle contrast for  
1013 HiLo microscopy optimization. *Optics Express* 19:14508-14517.

- 1014 Mertz J, Kim J (2010) Scanning light-sheet microscopy in the whole mouse brain with HiLo background  
1015 rejection. *J Biomed Opt* 15:016027-016027-7.
- 1016 Mertz J (2011) Optical sectioning microscopy with planar or structured illumination. *Nat Methods* 8:811-  
1017 819.
- 1018 Naka A, Adesnik H (2016) Inhibitory circuits in cortical layer 5. *Frontiers in Neural Circuits* 10:35.
- 1019 Packer AM, Russell LE, Dalgleish HW, Hausser M (2015) Simultaneous all-optical manipulation and  
1020 recording of neural circuit activity with cellular resolution *in vivo*. *Nat Meth* 12:140-146.
- 1021 Parot VJ, Sing-Long C, Adam Y, Boehm UL, Fan L, Farhi SL, Cohen AE (2019) Compressed hadamard  
1022 microscopy for high-speed optically sectioned neuronal activity recordings. *J Phys D: Appl Phys*  
1023 52:144001.
- 1024 Petreanu L, Huber D, Sobczyk A, Svoboda K (2007) Channelrhodopsin-2-assisted circuit mapping of long-  
1025 range callosal projections. *Nat Neurosci* 10:663-668.
- 1026 Podgorski K, Ranganathan G (2016) Brain heating induced by near-infrared lasers during multiphoton  
1027 microscopy. *J Neurophysiol* 116:1012-1023.
- 1028 Rickgauer JP, Deisseroth K, Tank DW (2014) Simultaneous cellular-resolution optical perturbation and  
1029 imaging of place cell firing fields. *Nat Neurosci* 17:1816-1824.
- 1030 Ronzitti E, Ventalon C, Canepari M, Forget BC, Papagiakoumou E, Emiliani V (2017) Recent advances in  
1031 patterned photostimulation for optogenetics. *Journal of Optics* 19:113001.
- 1032 Saganich MJ, Machado E, Rudy B (2001) Differential expression of genes encoding subthreshold-  
1033 operating voltage-gated K<sup>+</sup> channels in brain. *J Neurosci* 21:4609-4624.
- 1034 Saunders A, Johnson CA, Sabatini BL (2012) Novel recombinant adeno-associated viruses for cre  
1035 activated and inactivated transgene expression in neurons. *Front Neural Circuits* 6:47.
- 1036 Shemesh OA, Tanese D, Zampini V, Linghu C, Piatkevich K, Ronzitti E, Papagiakoumou E, Boyden ES,  
1037 Emiliani V (2017) Temporally precise single-cell-resolution optogenetics. *Nat Neurosci* 20:1796.
- 1038 Skocek O, Nöbauer T, Weilguny L, Traub FM, Xia CN, Molodtsov MI, Grama A, Yamagata M, Aharoni D,  
1039 Cox DD (2018) High-speed volumetric imaging of neuronal activity in freely moving rodents. *Nat Meth*  
1040 15:429-432.
- 1041 Sofroniew NJ, Flickinger D, King J, Svoboda K (2016) A large field of view two-photon mesoscope with  
1042 subcellular resolution for *in vivo* imaging. *eLife* 5:e14472.
- 1043 Szalay G, Judak L, Katona G, Ocsai K, Juhasz G, Veress M, Szadai Z, Feher A, Tompa T, Chiovini B, Maak P,  
1044 Rozsa B (2016) Fast 3D imaging of spine, dendritic, and neuronal assemblies in behaving animals.  
1045 *Neuron* 92.4:723-738.
- 1046 Ting JT, Lee BR, Chong P, Soler-Llavina G, Cobbs C, Koch C, Zeng H, Lein E (2018) Preparation of acute  
1047 brain slices using an optimized N-methyl-D-glucamine protective recovery method. *J Vis Exp* (132).  
1048 doi:10.3791/53825.

- 1049 Toomre D, Langhorst M, Davidson M Introduction to spinning disk confocal microscopy.
- 1050 Wu YW, Kim JI, Tawfik VL, Lalchandani RR, Scherrer G, Ding JB (2015) Input- and cell-type-specific  
1051 endocannabinoid-dependent LTD in the striatum. *Cell Rep* 10:75-87.
- 1052

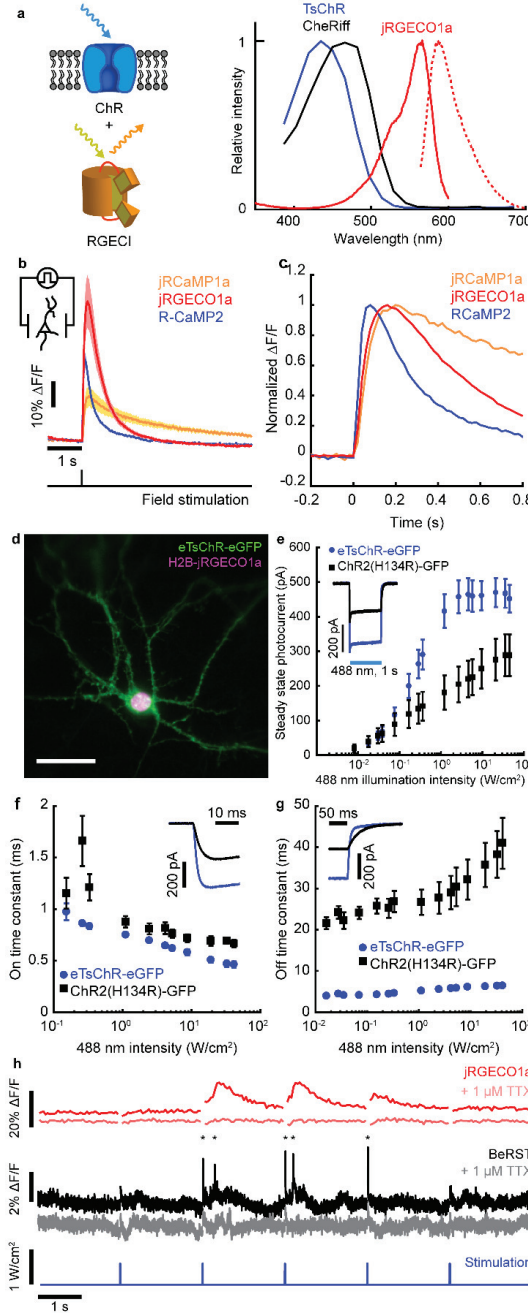


**Figure 1: All-optical neurophysiology with a blue-shifted channelrhodopsin and a red-shifted  $\text{Ca}^{2+}$  indicator.**

(a) Left: Schematic of a spectrally orthogonal channelrhodopsin and RGECl. Right: action spectra of proteins used in this work. Spectra are reproduced with permission from Dana, et al. *eLIFE* (2016) for jRGECO1a; Klapoetke, et al. *Nat. Meth.* (2014) for TsChR; and Hochbaum, et al. *Nat. Meth* (2014) for CheRiff.

(b) Single action potential responses of RGECl in cultured rat hippocampal neurons. Dark lines indicate the average of 3 FOVs, ~30 cells/FOV, for R-CaMP2 and 4 FOVs for jRGECO1a and jRCaMP1a. Colored bands indicate +/- s.e.m.. Dishes were stimulated with 1 ms field stimulation pulses. RGECl fluorescence was recorded at 50 Hz.

(c) Kinetics of the RGECl, shown by plotting data in (b) normalized to peak  $\Delta F/F$ .

(d) Cultured hippocampal neuron coexpressing H2B-jRGECO1a (magenta) and eTsChR (green). Scale bar 10  $\mu\text{m}$ .

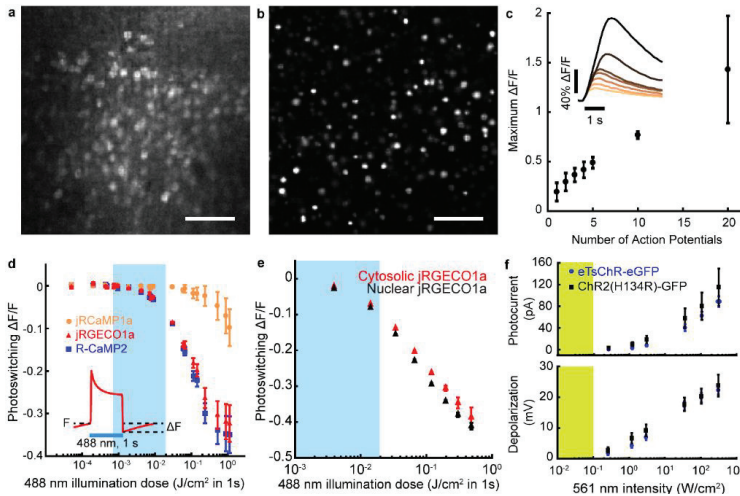
(e) Steady state photocurrents of eTsChR and ChR2(H134R) in cultured neurons held at -65 mV (1 s pulses, 488 nm, n = 6 cells for each construct). Inset: photocurrent response to 2  $\text{W}/\text{cm}^2$  488 nm illumination.

(f) Channelrhodopsin activation time constant as a function of 488 nm illumination intensity. Inset: photocurrents during illumination start.

(g) Closing time constants. Inset: photocurrents during illumination stop.

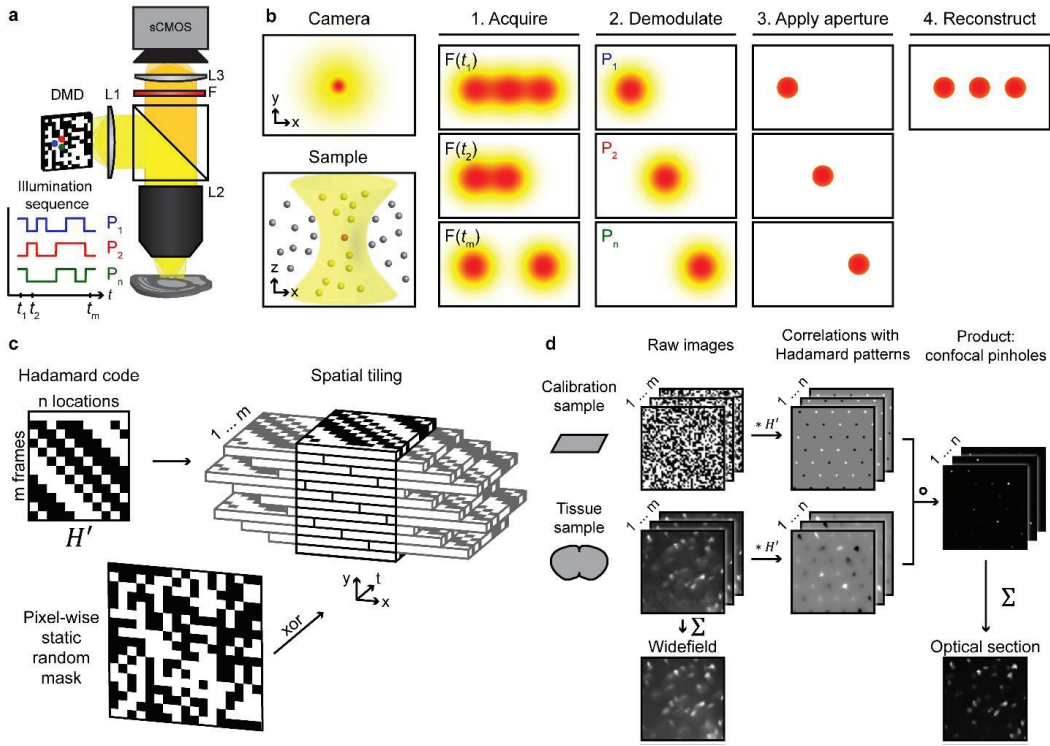
(h) Optogenetic stimulation induced action potentials and corresponding fluorescence transients in a cultured neuron expressing jRGECO1a and eTsChR. Pulses of blue light (488 nm, 10 ms, 680  $\text{mW}/\text{cm}^2$ ) drove action potentials (\*), which were identified via fluorescence of a far-red voltage-sensitive dye, BeRST1 (1  $\mu\text{M}$ , black)(Huang et al., 2015). Fluorescence transients of jRGECO1a accompanied action potentials (red). TTX (1  $\mu\text{M}$ ) silenced activity in both the voltage (pink) and  $\text{Ca}^{2+}$  (grey) channels, confirming that signals arose from neural activity and not optical crosstalk. Voltage imaging was performed at 500 Hz with 0.7  $\text{W}/\text{cm}^2$  640 nm light and calcium imaging was performed at 20 Hz with 1.1  $\text{W}/\text{cm}^2$  561 nm light. All error bars indicate mean +/- s.e.m..

1100



1101

**Figure 2: Characterization of soma-localized RGECl and eTsChR.** (a,b) Maximum intensity projections of Hadamard z-stacks from acute cortical slices prepared from mice injected with (a) cytosolic AAV1-syn-NES-jRGECO1a or (b) nuclear-targeted AAV9-syn-DO-H2B-jRGECO1a. Scale bars 100  $\mu m$ . (c) Maximum  $\Delta F/F$  of H2B-jRGECO1a fluorescence vs. number of evoked action potentials in cultured neurons, stimulated via current injection ( $n = 3$  cells). Inset: example responses to increasing numbers of action potentials. (d) Blue-light induced photoswitching of cytosolic RGECl in HEK293T cells under basal  $Ca^{2+}$  levels. RGECl fluorescence was recorded at 50 Hz with illumination at 561 nm, 80 mW/cm $^2$ . Blue illumination (1 s pulses, 488 nm) was added to the yellow illumination. Photoswitching was quantified as the decrease in fluorescence following blue light illumination compared to the initial fluorescence (inset),  $n = 3$  FOV, ~50 cells/FOV, for each construct. (e) Comparison of photoswitching in cytosolic and nuclear-localized jRGECO1a. Blue bar represents range of illumination doses used for optogenetic stimulation in this study. (f) Activation of channelrhodopsins as a function of 561 nm illumination intensity. Top: Steady state photocurrents in cultured neurons voltage clamped at -65 mV. Bottom: Voltage depolarization under current-clamp with an initial potential of -65 mV. Yellow bar indicates typical jRGECO1a imaging intensities. Acquired from cultured rat hippocampal neurons,  $n = 6$  for each construct. All error bars indicate mean +/- s.e.m..

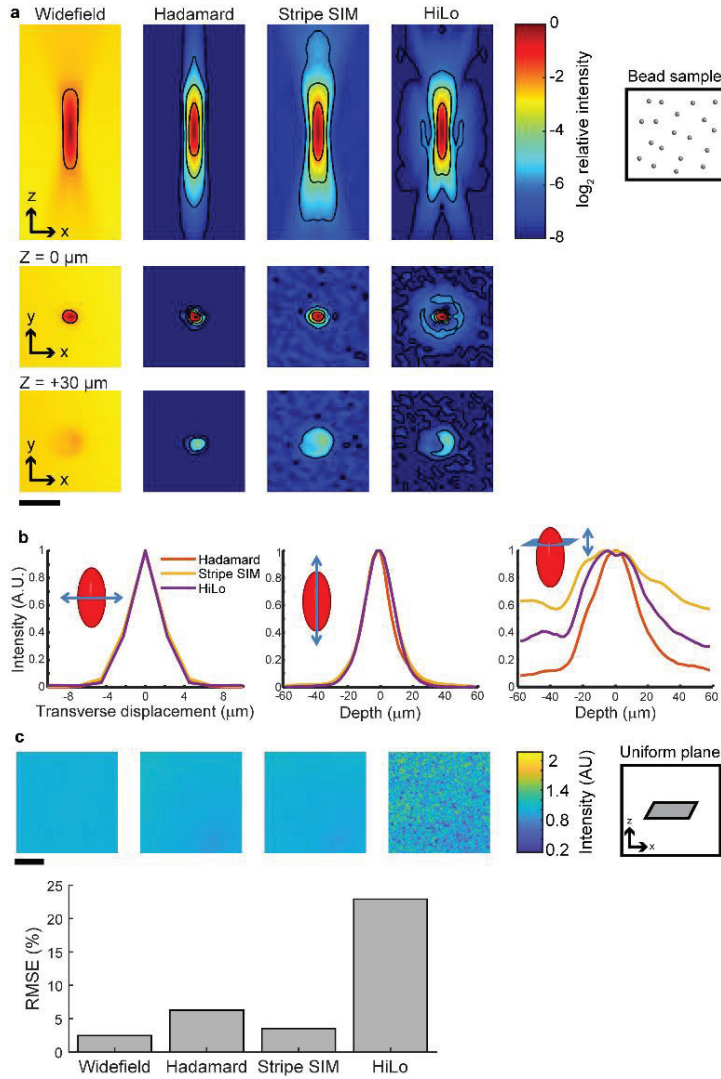


1118

1119

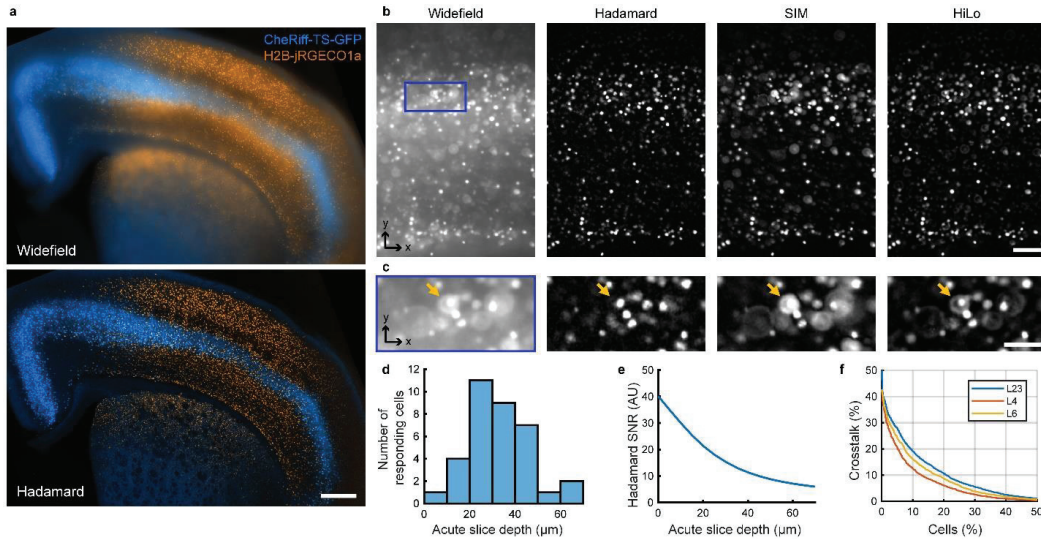
1120 **Figure 3: Optical sectioning by Hadamard microscopy.** (a) Schematic of ultra-widefield microscope,  
 1121 showing orthogonal illumination sequences in neighboring DMD pixels ( $P_1, P_2, \dots, P_n$ ). The full sequences  
 1122 have a 50% duty cycle. (b) Left: In a thick, scattering sample, the in-focus light (red) is dispersed by  
 1123 scattering and mixed with out-of-focus light (yellow). Right: Hadamard microscopy protocol. (1) The  
 1124 sample is illuminated with orthogonal functions of time at adjacent points in space. (2) The images are  
 1125 demodulated by matched filtering with the illumination sequence. (3) Scattered light is rejected by a  
 1126 software aperture. (4) The optically sectioned image is reconstructed from a sum of the demodulated  
 1127 images. (c) Codes from a Hadamard matrix were tiled to fill image space. The number of elements in the  
 1128 Hadamard code determined the number of frames in the pattern sequence. A random mask was applied  
 1129 to invert the code in 50% of illumination pixels, yielding pseudorandom patterns with flat spatial and  
 1130 temporal power spectra. (d) Raw images were acquired in a calibration sample (a thin homogeneous  
 1131 fluorescent film) and a tissue sample, one frame per Hadamard pattern. Cross-correlation maps  
 1132 between microscope data and Hadamard codes produced arrays of peaks corresponding to signals from  
 1133 distinct sample regions. Negative peaks corresponded to pixels whose Hadamard sequence was  
 1134 inverted. Pixel-wise multiplication of the demodulated images from the calibration sample and from the  
 1135 tissue sample led to multi-point confocal images. These images were summed to produce an image  
 1136 reconstruction. Detailed description in **Methods**.

1137

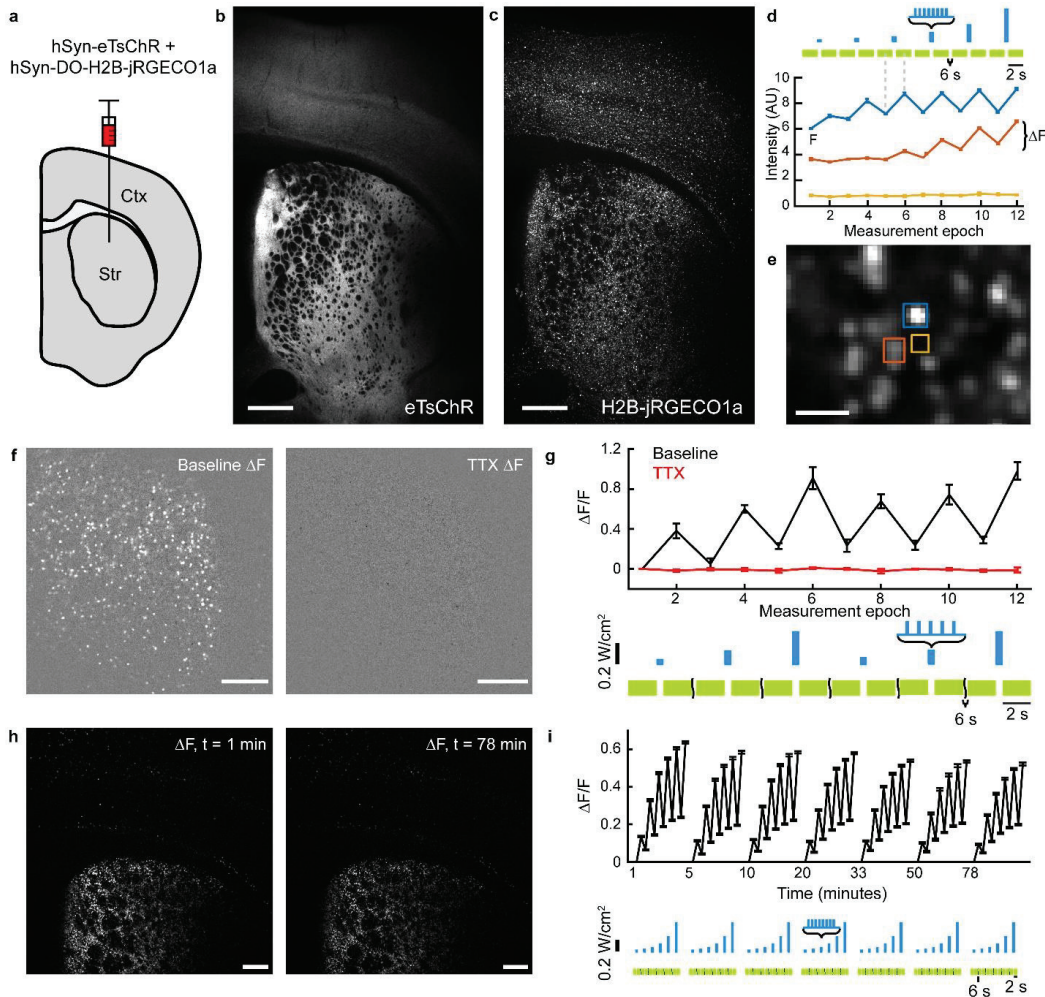


1138  
1139 **Figure 4: Characterization of Hadamard Microscopy.** (a-b) Comparison of structured illumination  
1140 microscopy (SIM) optical sectioning methods using sub-diffraction beads. (a) Images show (left to right):  
1141 Wide-field epifluorescence, Hadamard microscopy using 12 patterns, stripe SIM with period 4 pixels and  
1142 four phases, and HiLo microscopy using DMD-projected pseudorandom patterns. Top row: Radially  
1143 averaged meridional cross-section of the point-spread function (PSF). Second row: transverse cross-  
1144 section at the focal plane. Third row: transverse cross-section at 30 μm defocus. For all (a) the color  
1145 scale is logarithmic, and contours were drawn on every 4-fold change in intensity. Scale bar is 20 μm,  
1146 isotropic. (b) (Left and center) Lateral and axial line profiles through the PSF show equivalent resolution  
1147 for the three sectioning methods. (Right) Integrated intensity in transverse cross-sections reveals off-  
1148 axis spurious side lobes in stripe SIM and HiLo which contribute to out-of-focus crosstalk. (c) A uniform  
1149 fluorescent plane at the focal plane resulted in larger inhomogeneities when imaged using HiLo in  
1150 comparison with the other methods, a consequence of inhomogeneities in HiLo illumination(Mazzaferrri

1151 et al., 2011). The fractional noise in HiLo did not decrease with increasing photon counts. Top: Optical  
 1152 section images of the uniform plane, all shown at the same linear color scale. Bottom: Deviations from  
 1153 uniformity in the images on top. Hadamard and stripe SIM microscopies avoided this artifact by  
 1154 providing illumination whose time-average intensity was precisely the same at all sample points. Scale  
 1155 bar 200  $\mu\text{m}$ . For all panels, each sample was imaged in matched conditions for all methods (number of  
 1156 images, illumination intensity, acquisition time). Detailed description in **Methods**.  
 1157

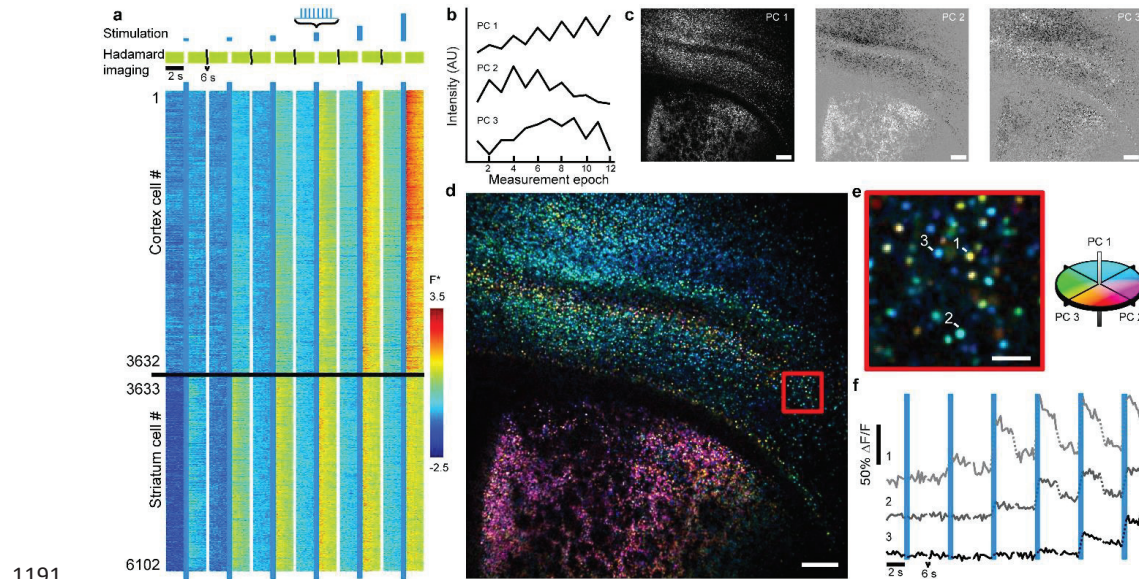


1158  
 1159 **Figure 5: Hadamard microscopy resolves individual H2B-jRGECO1a labeled neurons in acute brain**  
 1160 **slices.** (a) Two-color fluorescence maximum-intensity projections acquired from an acute brain slice  
 1161 expressing H2B-jRGECO1a broadly in cortex and striatum and membrane targeted CheRiff-TS-GFP in L5  
 1162 pyramidal cells. Top: wide-field epifluorescence. Bottom: Hadamard image. Scale bar 500  $\mu\text{m}$ . (b) Images  
 1163 acquired with different 1P computational optical sectioning methods. Images were acquired in the same  
 1164 sample with matched conditions (number of images, illumination intensity, acquisition time). The  
 1165 sample comprised an acute brain slice expressing H2B-jRGECO1a. Images show (left to right): Wide-field  
 1166 epifluorescence, Hadamard microscopy using 12 patterns, SIM with period 4 pixels and four phases, and  
 1167 HiLo microscopy using DMD-projected speckle patterns. Scale bar 100  $\mu\text{m}$ . The blue box region is  
 1168 expanded in (c). (c) Hadamard microscopy avoids defocus lobes present using other methods. The  
 1169 orange arrows indicate a defocused cell that is rejected by Hadamard microscopy but appears in the  
 1170 other techniques. All images use the same linear scale of normalized grey values. Scale bar 50  $\mu\text{m}$ . (d)  
 1171 Depth distribution of responsive cells during Hadamard functional recording, measured by high  
 1172 resolution confocal microscopy acquired after the functional measurement and registered to the  
 1173 Hadamard images. The depth was  $32.2 \pm 12.7 \mu\text{m}$  (mean  $\pm$  std. dev.,  $n = 35$  neurons). (e) Depth-  
 1174 dependent decay in SNR for Hadamard microscopy in acute slices. Decay length was  $\sigma_z = 27 \mu\text{m}$ . (f)  
 1175 Estimated distribution of crosstalk in neuronal recordings using Hadamard microscopy. Only 10% of cells  
 1176 had more than 20% crosstalk (fluorescence attributable to other cells) in L2/3 (**Methods**).  
 1177



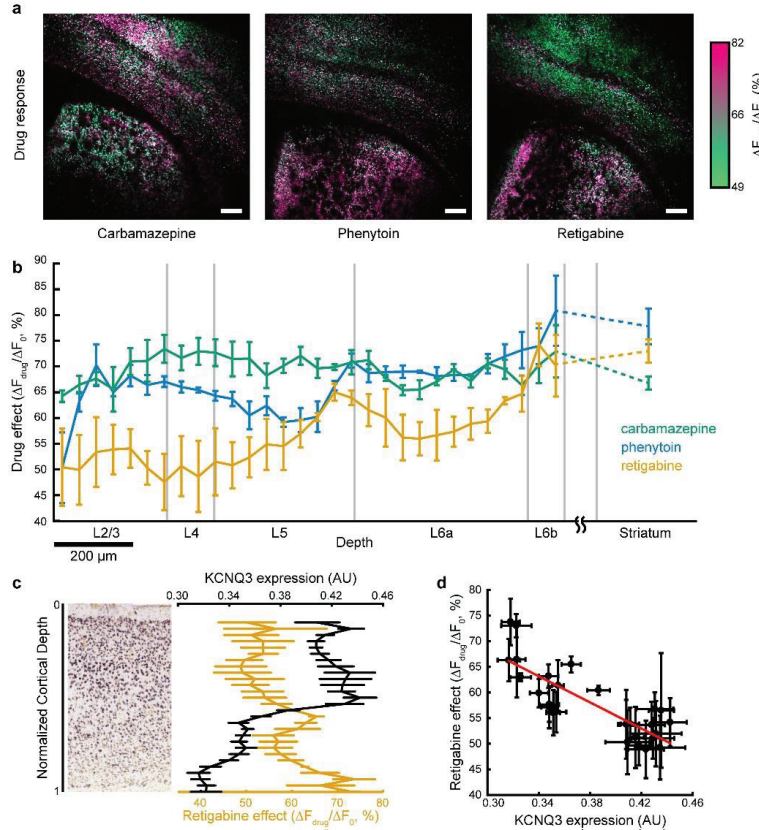
1177  
1178  
1179  
1180  
1181  
1182  
1183  
1184  
1185  
1186  
1187  
1188  
1189  
1190

**Figure 6: Ultra-widefield AON in acute brain slices.** (a) AAV9 viruses coding for hSyn-eTsChR and hSyn-DO-H2B-jRGECO1a were co-injected in neonatal mouse cortex and striatum. (b) Maximum intensity projection of a Hadamard z-stack of eTsChR expression in a coronal corticostriatal slice from a P21 mouse. (c) Same as (b) in the H2B-jRGECO1a channel. (d) Fluorescence traces from regions indicated in (e). Two cells showed optogenetically induced fluorescence transients, while a region between the cells showed no signal. Here the sets of 11 images acquired before and after each optogenetic stimulus were averaged to form single pre- and post-stimulus fluorescence values. Error bars represent s.e.m. over  $n = 11$  Hadamard images. Scale bar 25  $\mu\text{m}$ .  $F$  is defined as the average intensity of the first imaging epoch and  $\Delta F$  is the signal increase following blue light stimulation. (d) Magnified view of region of Fig. 3e showing single-cell resolution.



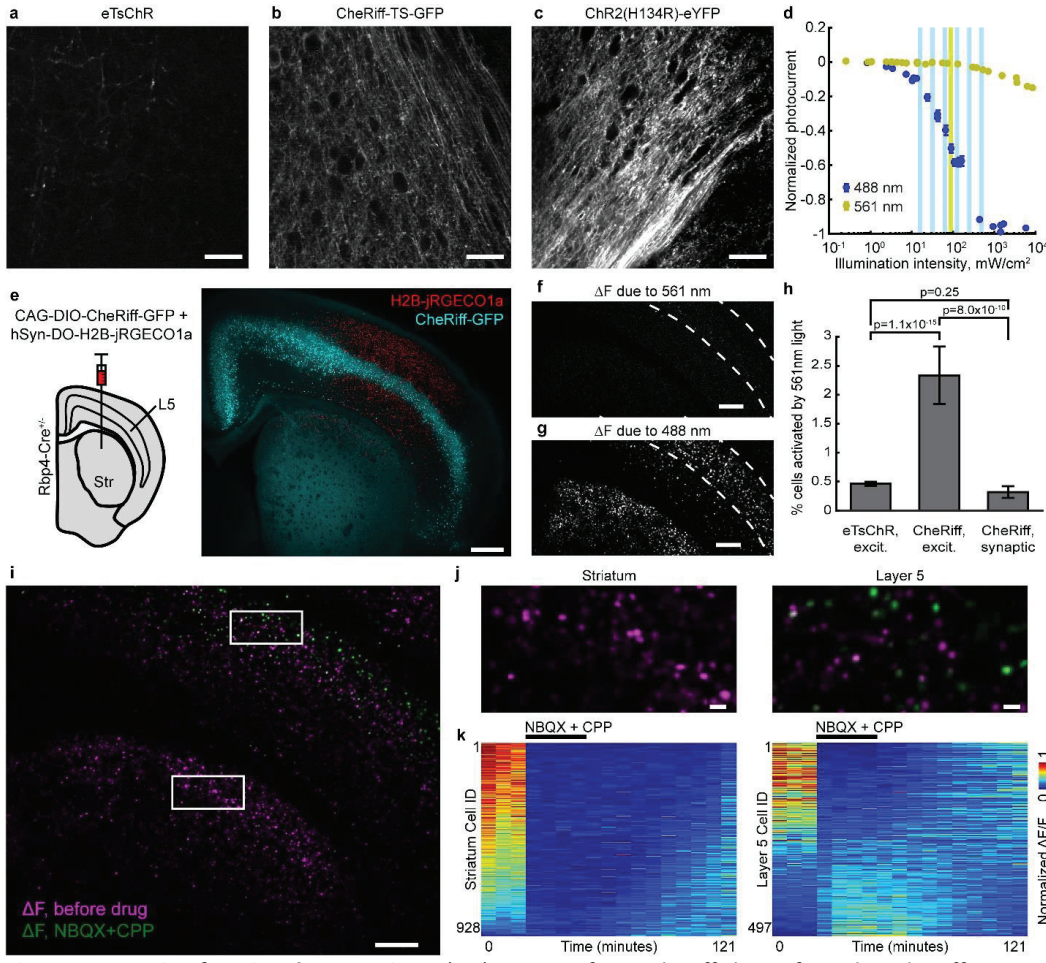
1191  
1192  
1193 **Figure 7: Ultra-widefield AON in acute brain slices.** (a) Top: Stimulation and imaging protocol. An FOV  
1194 spanning cortex and striatum was stimulated with eight 5 ms pulses of 488 nm light at 20 Hz with  
1195 intensities of 15, 30, 60, 120, 240, and 480 mW/cm<sup>2</sup>. Bottom: heat map of 6,102 single-cell fluorescence  
1196 traces acquired simultaneously. Individual fluorescence intensities traces were normalized as  $F^* = (F -$   
1197  $\text{mean}(F))/\text{std}(F)$ . White breaks separate measurements at different optogenetic stimulus intensities.  
1198 Imaging was performed at 5.6 Hz with 100 mW/cm<sup>2</sup> 561 nm light. (b) Waveforms of main principal  
1199 components from  $n = 31,754$  cells. See Methods for additional details. (c) Principal components from (a)  
1200 projected into pixel space. (d) Image of the slice recorded in (a) with cells colored by the principal  
1201 component amplitudes of the functional responses. (e) Close-up of the red boxed region of (d). (f) Three  
1202 example single-cell fluorescence traces. Dotted lines indicate pauses in Hadamard imaging (400 ms  
1203 during optogenetic stimulation, 6 s between stimuli).  $\Delta F/F$  is defined relative to the intensity in the first  
1204 imaging epoch. Scale bars 250  $\mu\text{m}$  in (c, d) and 50  $\mu\text{m}$  in (e).

1205  
1206



1207  
1208 **Figure 8: Mapping effects of anti-epileptic drugs (AEDs) on excitability.** (a) Maps of AED effects on  
1209 excitability. Slices were measured using the excitability protocol as in Fig. 7. The protocol was repeated  
1210 five times before drug addition and four times after addition of carbamazepine (100  $\mu$ M), phenytoin  
1211 (100  $\mu$ M), or retigabine (25  $\mu$ M). The ratio of mean optogenetically induced change in fluorescence for  
1212 each cell before ( $\Delta F_0$ ) and after drug addition ( $\Delta F_{\text{drug}}$ ) is encoded as color in a green to pink axis. Scale  
1213 bars 250  $\mu$ m. (b) Average drug response ( $\Delta F_{\text{drug}}/\Delta F_0$ ) as a function of cortical depth for  $n = 3$  slices for  
1214 each drug. All striatal cells in a slice were pooled into a single bin. Data represents  $n = 9,793$  cells for  
1215 carbamazepine, 11,858 cells for phenytoin, and 10,103 cells for retigabine. Error bars represent s.e.m.  
1216 over  $n = 3$  slices for each drug. (c) Left: *in situ* hybridization image from Allen Brain Atlas experiment  
1217 #100041071 showing KCNQ3 expression in somatosensory cortex of a P28 mouse. Right: cortical depth  
1218 dependence of retigabine drug effect (same as Fig. 4b) and KCNQ3 expression level determined from *in*  
1219 *situ* hybridization images of  $n = 11$  slices from the Allen Brain Atlas. (d) Data from (c) showing effect of  
1220 retigabine on excitability vs. KCNQ3 expression. Best fit line is indicated in red. Error bars indicate s.e.m.,  
1221 treating each slice as an independent measurement.

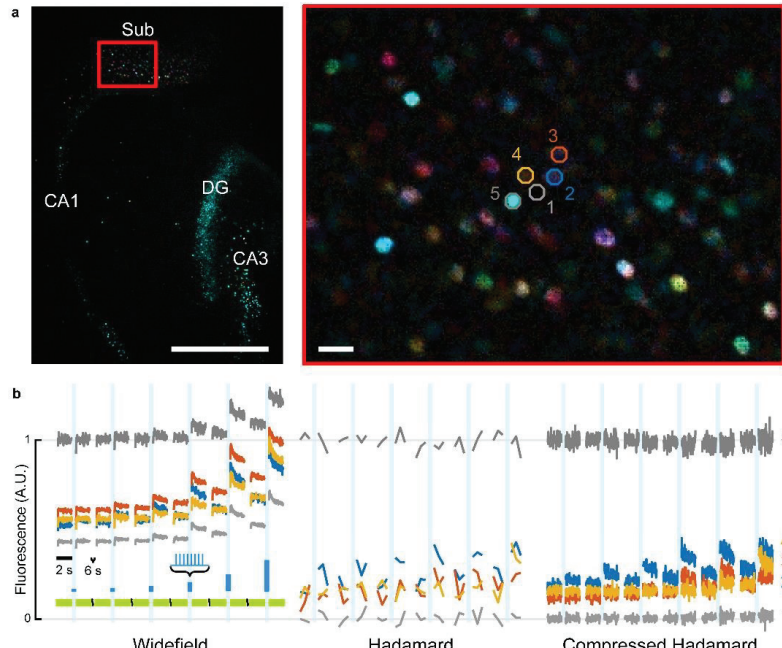
1222



1223  
1224 **Figure 9: Mapping functional connections.** (a-c) Images of axonal trafficking of eTsChR, CheRiff-TS-GFP,  
1225 and ChR2(H134R)-YFP, scaled to the same counts. Equal volumes of AAV2/9-hSyn-ChR2(H134R)-eYFP,  
1226 AAV2/9-hSyn-CheRiff-TS-GFP, and AAV2/9-hSyn-eTsChR were injected in the left hemisphere in separate  
1227 mice and coronal slices of the contralateral hemisphere were prepared after > 4 weeks. Images were  
1228 acquired near the corpus callosum with 2-photon microscopy. Scale bars 50  $\mu$ m in (a-c). (d) Comparison of CheRiff  
1229 photocurrents in HEK293T cells induced by yellow (561 nm) and blue (488 nm) light. Vertical  
1230 bars indicate intensities used in acute slice experiments. The blue illumination intensity to achieve 50%  
1231 activation was 94 mW/cm<sup>2</sup> (88, 99 mW/cm<sup>2</sup> 95% confidence interval, n = 7 HEK cells). (e) Left: viral  
1232 constructs for mapping functional connections. Cre-dependent AAV9-CAG-DIO-CheRiff-GFP and AAV9-  
1233 hSyn-DO-H2B-jRGECO1a were co-injected in Rbp4-Cre<sup>+/−</sup> neonatal mice. Right: at P21, CheRiff-GFP  
1234 expressed in Cre<sup>+</sup> L5 pyramidal cells, including corticostriatal projection neurons. H2B-jRGECO1a  
1235 expressed broadly in cortex and striatum. Image represents a maximum intensity projection of a  
1236 Hadamard z-stack. Scale bar 500  $\mu$ m. (f) CheRiff activation by yellow (561 nm, 100 mW/cm<sup>2</sup>) light. The  
1237 image shows the difference between mean fluorescence of H2B-jRGECO1a in the 2<sup>nd</sup> and 1<sup>st</sup> second  
1238 after onset of yellow light for Ca<sup>2+</sup> imaging. Image represents a mean of n = 3 repetitions of the  
1239 measurement. Spurious CheRiff activation would cause neural firing, which would lead to an increase in

1240 H2B-jRGECO1a fluorescence. (g) Mean  $\Delta F$  induced by blue light stimulation, averaged over three runs.  
1241 (g) and (h) are scaled identically. Scale bars 250  $\mu\text{m}$  in (f,g). Dashed lines in (f-g) indicate Layer 5 of the  
1242 cortex. (h) Comparison of optical crosstalk for different optogenetic actuators and protocols, as  
1243 measured by percent of cells showing  $\text{Ca}^{2+}$  transients in response to onset of illumination with 561 nm  
1244 light for fluorescence imaging. The three conditions corresponded to eTsChR in the excitability assay  
1245 (co-expression of actuator and reporter in the same neurons), CheRiff in the excitability assay, and  
1246 CheRiff in the functional connectivity assay (mutually exclusive expression of actuator and reporter).  
1247 Error bars are calculated assuming a Poisson distribution with  $s.e.m = \sqrt{n_{active}}/n_{total}$ . (i) Mean  
1248 optogenetically induced fluorescence transients,  $\Delta F$ , before (magenta) and after (green) addition of  
1249 excitatory blockers, NBQX (10  $\mu\text{M}$ ) and CPP (10  $\mu\text{M}$ ). Stimulation and imaging were performed as in Fig.  
1250 7. Images are the median of 3 runs before and 4 runs after adding excitatory blockers. Scale bar 250  $\mu\text{m}$ .  
1251 (j) Magnified views of indicated regions in striatum and Layer 5 in (i). Scale bar 25  $\mu\text{m}$ . (k) Mean  
1252 optogenetically induced fluorescence response,  $\Delta F$ , for each cell before, in the presence of, and during  
1253 washout of excitatory blockers. Left: striatum. Right: Layer 5. Each column represents the mean  
1254 optogenetically induced  $\Delta F$  of an experimental protocol as in Fig. 7a. The slice was measured over 121  
1255 minutes (5-10 minutes between measurements, 22 minutes before last measurement). For visualization,  
1256 each cell trace was normalized by its mean.  
1257

1258



1259

1260

1261

1262

1263

1264

1265

1266

1267

1268

1269

1270

1271

1272

1273

1274

1275

**Figure 10: High-speed wide-area all-optical neurophysiology using Compressed Hadamard Imaging.**

(a) Left: PCA-colored map showing response of nuclear jRGECO1a to stepped optogenetic stimulation across the hippocampal formation. Sub: Subiculum, DG: Dentate gyrus, CA1/CA3: Cornu ammonis. Scale bar 0.5 mm. Right: Magnified view of the cyan rectangle shows the location of a background region (1, gray), three responding cells (2-4, colored), and a bright, non-responding cell (5, gray). Scale bar 20  $\mu$ m. Color saturation was increased by 100% for display. (b) Comparison of fluorescence traces extracted from ROIs in (a) from the same recording, using three different analyses. Amplitude was scaled to normalize the baseline intensity of the brightest ROI. Left: Widefield data calculated as the sum of paired complementary patterns. Signals had a time resolution of 33 Hz, but included out-of-focus background. Camera framerate was 66 Hz. Middle: Conventional Hadamard analysis produced one optical section every 48 frames, possibly with errors due to changing cell intensities during the pattern period. Right: Compressed Hadamard analysis obtained high-speed optically sectioned movies with 33 Hz framerate. Both Hadamard optical sections show a zero-centered value for the background ROI (1) and flat brightness for a non-responding cell (5), but distinct optogenetic activation thresholds for each responding cell (2-4).

Construct	Single AP max ΔF/F (%)	$\tau_{on}$ (ms)	$\tau_{off}$ (ms)	$\tau_{bleach}$ (s)
jRGECO1a	54 ± 10, n = 4 FOV, ~30 cells/FOV	47.2 ± 1.0	443 ± 38	80.5 ± 5.1, n = 9 cells
R-CaMP2	31 ± 3, n = 3 FOV, ~30 cells/FOV	26.3 ± 1.0	271 ± 20	61.9 ± 2.8, n = 8 cells
jRCaMP1a	17 ± 4, n = 4 FOV, ~30 cells/FOV	61.2 ± 2.1	1600 ± 160	37.8 ± 2.1, n = 8 cells

1276      **Table 1: *In vitro* characterization of RGEClS.** Quantification of action potential responses in cultured  
 1277      neurons in Fig. 1, and photobleaching kinetics in HEK293T cells. Action potential magnitudes and sensor  
 1278      kinetics are from 3 FOVs for R-CaMP2 and 4 FOVs for jRGECO1a and jRCaMP1a in separate dishes.  
 1279      Dishes were stimulated with 1 ms field stimulation pulses while imaging RGECl fluorescence at 50 Hz  
 1280      with 2.45 W/cm<sup>2</sup> 561 nm illumination. Photobleaching measurements were performed in HEK293T cells  
 1281      under 44 W/cm<sup>2</sup> 561 nm illumination (compared to 0.1 W/cm<sup>2</sup> used in slice imaging). All values are  
 1282      reported as mean ± s.e.m..  
 1283

1284

	eTsChR	ChR2(H134R)-GFP	p-value, Student's t-test
Access resistance (MΩ)	12.3 ± 1.5	12.4 ± 1.3	0.96
Membrane resistance (MΩ)	633 ± 84	467 ± 88	0.20
Membrane capacitance (pF)	36.5 ± 4.8	44.9 ± 9.7	0.45
Resting potential (mV)	-36.5 ± 4.8	-44.3 ± 2.9	0.13

1285      **Table 2: Patch characterization of eTsChR.** Patch parameters of cells in Fig. 1. All values are reported as  
 1286      mean ± s.e.m., n = 6 cells throughout.  
 1287

1288